Adsorption and Diffusion of CH4, N2, and Their Mixture in MIL-101(Cr): A Molecular Simulation Study

Adsorption and Diffusion of CH_4, N_2 and their Mixture in MIL-101(Cr): A Molecular Simulation Study

Yimin Shao,[1] Shanshan Wang,[2] Liangliang Huang,[3*] Shenghong Ju,[4] Xianfeng Fan, [1] Wei Li[1*]

1. Institute for Materials and Processes, School of Engineering, The University of Edinburgh, Edinburgh EH9 3FB, Scotland, UK
2. College of Chemical Engineering, International Innovation Center for Forest Chemicals and Materials, Nanjing Forestry University, Nanjing, Jiangsu 210037, P.R. China
3. School of Chemical, Biological and Materials Engineering, University of Oklahoma, Norman, Oklahoma 73019, United States
4. China-UK Low Carbon College, Shanghai Jiao Tong University, Shanghai 201306, China

Abstract

A comprehensive quantitative grasp of methane (CH_4), nitrogen (N_2), and their mixture's adsorption and diffusion in MIL-101(Cr) is crucial for wide and important applications, e.g. natural gas upgrading, coal-mine methane capturing. Previous studies often overlook the impact of gas molecular configuration and MIL-101 topology structure on adsorption, lacking quantitative assessment of primary and secondary adsorption sites. Additionally, understanding gas mixture adsorption mechanisms remains a research gap. To bridge this gap and to provide new knowledge, we utilized Monte Carlo and molecular dynamics simulations for computing essential MIL-101 properties, encompassing adsorption isotherms, density profiles, self-diffusion coefficients, radial distribution function (RDF), and CH_4/N_2 selectivity. Several novel and distinctive findings are revealed by the atomic-level analysis, including 1) the significance of C=C double bond of the benzene ring within MIL-101 for CH_4 and N_2 adsorption, with Cr and O atoms also exerting notable effects. 2) Density distribution analysis reveals CH_4's preference for large and medium cages, while N_2 is evenly distributed along pentagonal and triangular window edges and small tetrahedral cages. 3) Calculations of self-diffusion and diffusion activation energies suggest N_2's higher mobility within MIL-101 compared to CH_4. 4) In the binary mixture, the existence of CH_4 can decrease the diffusion coefficient of N_2. In summary, this investigation provides valuable microscopic insights into the adsorption and diffusion phenomena occurring in MIL-101, thereby contributing to a comprehensive understanding of its potential for applications, e.g. natural gas upgrading, selective capture of coal-mine methane.

Keywords: MIL-101, Methane, Adsorption, CH_4/N_2 selectivity, Molecular simulation

Graphical Abstract

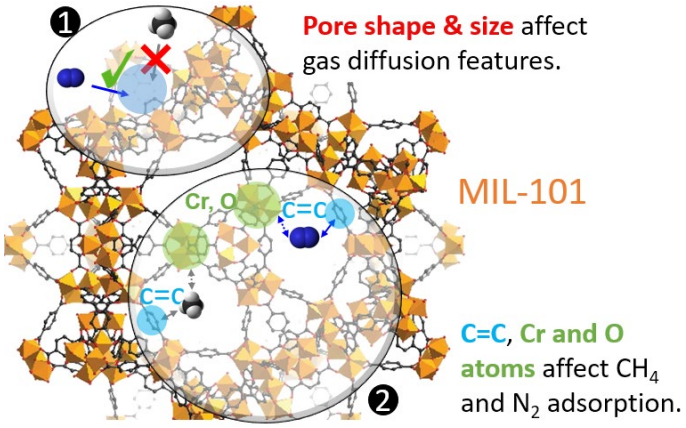

1. Introduction

Global warming, resulting from the escalating levels of greenhouse gases, represents an undeniable and urgent challenge in the twenty-first century [1]. Methane (CH_4), one of the six primary greenhouse gases regulated by the Kyoto Protocol, possesses a warming potential over 20 times greater than that of carbon dioxide (CO_2) [2]. Annual methane emissions from underground coal mines have exhibited a range of 2.03 to 2.87 billion cubic meters in recent decades [3]. Projections by the US Environmental Protection Agency forecast that global methane emissions from coal mines will surpass 784.3 MtCO2e by 2030 [4]. Furthermore, coal-mine methane, with its low CH_4 content (50%), is unsuitable for direct utilization as chemicals or fuels [5]. Consequently, the selective separation of CH_4 from N_2 in coal-mine methane holds immense significance and vitality. This separation process has the potential to not only yield valuable chemicals and fuels, leading to economic benefits but also contribute to the reduction of atmospheric greenhouse gas emissions, thereby aiding in the fight against global warming [6].

The cryogenic distillation process, which relies on the difference in boiling temperatures between CH_4 (112 K) and N_2 (77 K) to separate CH_4 from N_2 in coal-mine methane, is the most widely employed in industry [7]. However, this approach is deemed economically impractical, energy-intensive, and environmentally unfavourable for coal-mine methane capture. This is primarily due to the low CH_4 content in coal-mine methane and the demanding operating conditions, such as low temperatures and high pressures, required for cryogenic distillation [8]. An alternative approach gaining significant attention is adsorption separation, which employs porous materials and operates at ambient temperature and pressure. This method is widely recognized as an energy-efficient and cost-effective solution for capturing low-concentration CH_4 from N_2 in coal-mine methane [9].

Extensive research has been conducted on conventional porous materials, including activated carbons [10], zeolites [11], and molecular sieves [12], to evaluate their effectiveness in separating CH_4/N_2 mixtures. However, the challenge of achieving high CH_4/N_2 selectivity remains unresolved. To address this issue, it is imperative to explore novel types of porous materials. Metal-organic frameworks (MOFs) have emerged as promising candidates for selective gas separations due to their tuneable pore size and chemistry [13]. Several MOFs have been investigated for CH_4/N_2 separation, such as ZIFs [14], Cu-MOFs [15], Al-MOFs [7], and Zr-MOFs [16]. Among them, MIL-101(Cr), a Cr-based MOF composed of chromium ions and terephthalic

acid ligands, holds significant potential for gas adsorption applications. MIL-101(Cr) possesses unsaturated Lewis acid sites, an exceptionally high specific surface area, large pore size, significant pore volume, superior separation selectivity, ease of regeneration, and excellent thermal, chemical, and water stability [17].

While numerous experimental studies investigated the adsorption of individual N_2 and CH_4 gases using various MIL-101 modifications such as MIL-101(Cr) [18, 19], CH_3- MIL-101(Cr) and NO_2-MIL-101(Cr) [20], NH_2-MIL101(Al) [21], NH_2-MIL101(Cr) [22] and NH_2-MIL101(Fe) [23], few theoretical studies have been conducted to investigate this area. Zhang et al. [18] utilized Density functional theory (DFT) to compare the electron cloud density and its effects on N_2 adsorption for different functional group-modified MIL-101 structures, which ignored many key information of N_2 adsorption mechanism, such as MIL-101 topological structure and molecular sieving effect. Sedighi et al. [24] analyzed N_2 adsorption sites using snapshots and RDF through molecular simulation, but they did not analyze from the RDF that the C=C bond of the linker of MIL-101 is also one of the adsorption sites, and did not quantitatively compare the effects of different adsorption sites. Teo et al.[25] analyzed the spatial distribution of CH_4 in MIL-101 from snapshots, the analysis with only snapshots was not very comprehensive to understand CH_4 adsorption in MIL-101. Although Liu et al. [26] performed molecular simulation to explore the spatial distribution of CH_4 in MIL-101, they did not explain the reason why CH_4 has such a distribution. Additionally, they used a united-atom model with one site to represent CH_4, which ignored the impact of molecular configuration (e.g. C-H bonds [27], molecular space orientations, octopole moment [28]) on the spatial distribution during mutation. And there was no quantitative analysis of which atomic structures played a major and secondary role in the adsorption of CH_4.

Ji Woong Yoon [29, 30] et al. reported that the trend of preferential adsorption of CH_4 versus N_2 on MIL-101 reverses, when the preheating temperature of MIL-101(Cr) synthesis process was increased to 523K. These studies did not provide an in-depth analysis of adsorption mechanism for CH_4 and N_2. For example, Ji Woong Yoon et al. did not describe the details about how to analyze the adsorption sites of CH_4 in the entire text. Thus, it remains open to debate whether the conclusion is fully substantiated that the primary adsorption site for CH_4 is in close proximity to the metallic element Cr. Furthermore, to align with their special experimental findings, Ji Woong Yoon et al. [30] computed new force field parameters specifically tailored to match the experimental data. By adjusting the force field parameters for N_2, Ji Woong Yoon et

al. examined that the primary adsorption site for N_2 is in close proximity to the metallic element Cr. However, it's important to note that this assertion may not hold true universally. Ji Woong Yoon et al. also used snapshots to observe the distance between the metal and N_2 to identify the main adsorption sites. This analytical approach appears to be heavily biased or lacking in considering multiple perspectives. Additionally, the studies of Ji Woong Yoon et al. did not quantitatively compare the effects of different adsorption sites, and ignored the influence of the special topological structure of MIL-101(Cr) on the adsorption of CH_4 and N_2.

Therefore, these theoretical studies failed to consider the influence of the molecular radius and MIL-101(Cr) topology structure of CH_4 and N_2 on adsorption behavior and lacked a quantitative analysis of the significant and secondary roles played by specific atomic structures in the adsorption of CH_4 and N_2. As a result, a comprehensive understanding of the detailed adsorption behavior of CH_4 and N_2 on MIL-101 is still required.

Limited experimental research has been conducted on the utilization of MIL-101(Cr) for the adsorption and separation of CH_4/N_2 mixtures. Zhang et al. conducted experiments on the synthesis of MIL-101(Cr) and investigated its N_2 and CH_4 adsorption equilibrium and CH_4/N_2 separation capabilities [31]. The experimental data demonstrated that the N_2 and CH_4 adsorption isotherms conformed to the Langmuir model. The selectivity for CH_4/N_2 separation ranged from 2.6 to 3.3, varying with changes in temperature and pressure. Another study by Li et al. examined the impact of Mg^{2+} doping on the pore structure of MIL-101 and its adsorption selectivity for CH_4/N_2 gas mixtures [32]. The findings indicated that Mg^{2+} doping enhanced the adsorption capacity of both CH_4 and N_2, as well as the selectivity for CH_4/N_2 separation. This effect was attributed to the inhibition of hydrogen bond formation resulting from the appropriate amount of Mg^{2+} doping, which positively influenced CH_4 adsorption. Furthermore, Zhang et al. explored the modification of MIL-101 through the addition of $-NO_2$ and $-CH_3$ functional groups to alter the selectivity of CH_4/N_2 separation [20]. Experimental results revealed that $-NO_2$ exhibited a greater separation effect on CH_4/N_2 than $-CH_3$, with a selectivity of 2.8 at 298 K, 1 bar. Additionally, the diffusion of molecules in porous materials plays an important role in many chemical processes, such as shape selective catalysis, molecular sieving and selective adsorption. With better understanding of the complexities of gas diffusion in porous materials, it is necessary for the design, development, and optimization of catalysis and adsorption [33]. In adsorption processes, diffusion governs the rate of adsorption-desorption cycles in adsorption-based processes and directly impacts the selectivity of products in gas

separations [34]. So, there is a lack of further explanation of mixture diffusion and adsorption at the microscopic level.

In this study, the primary objective is to employ grand canonical Monte Carlo (GCMC) and molecular dynamics (MD) simulation methods to gain a comprehensive understanding of the influence of structural variations in the MIL-101 framework on the adsorption and diffusion of CH_4 and N_2 gases within its pores. The research aims to address three fundamental questions, as illustrated in Figure S1: (I) What are the adsorption and diffusion behaviors of single-component CH_4 and N_2 in MIL-101? (II) How do the adsorption and diffusion behaviors differ in the presence of two-component CH_4 and N_2 in MIL-101? (III) Are the adsorption behaviors of the single-component and two-component systems interconnected?

Accordingly, the article is divided into two parts: the analysis of the single-component system and the analysis of the two-component system. Before the analysis in Parts 1 and 2, for single-component gases, it is necessary to verify the reliability of the simulation and validate the force filed through the adsorption isotherm and isosteric heat. In the case of the two-component system, the reliability of the simulation is assessed by analyzing the selectivity of CH_4/N_2, which enables a more comprehensive investigation of the adsorption and diffusion behaviors. The analysis primarily utilizes three methods: density distribution profile, self-diffusion coefficients, and RDF. By elucidating the mass transport characteristics of CH_4 in MIL-101 with varying N_2 concentrations at the atomic level, this study provides valuable theoretical insights for the separation of CH_4/N_2 mixtures using MIL-101(Cr).

2. Methods

2.1 Grand Canonical Monte Carlo Simulations

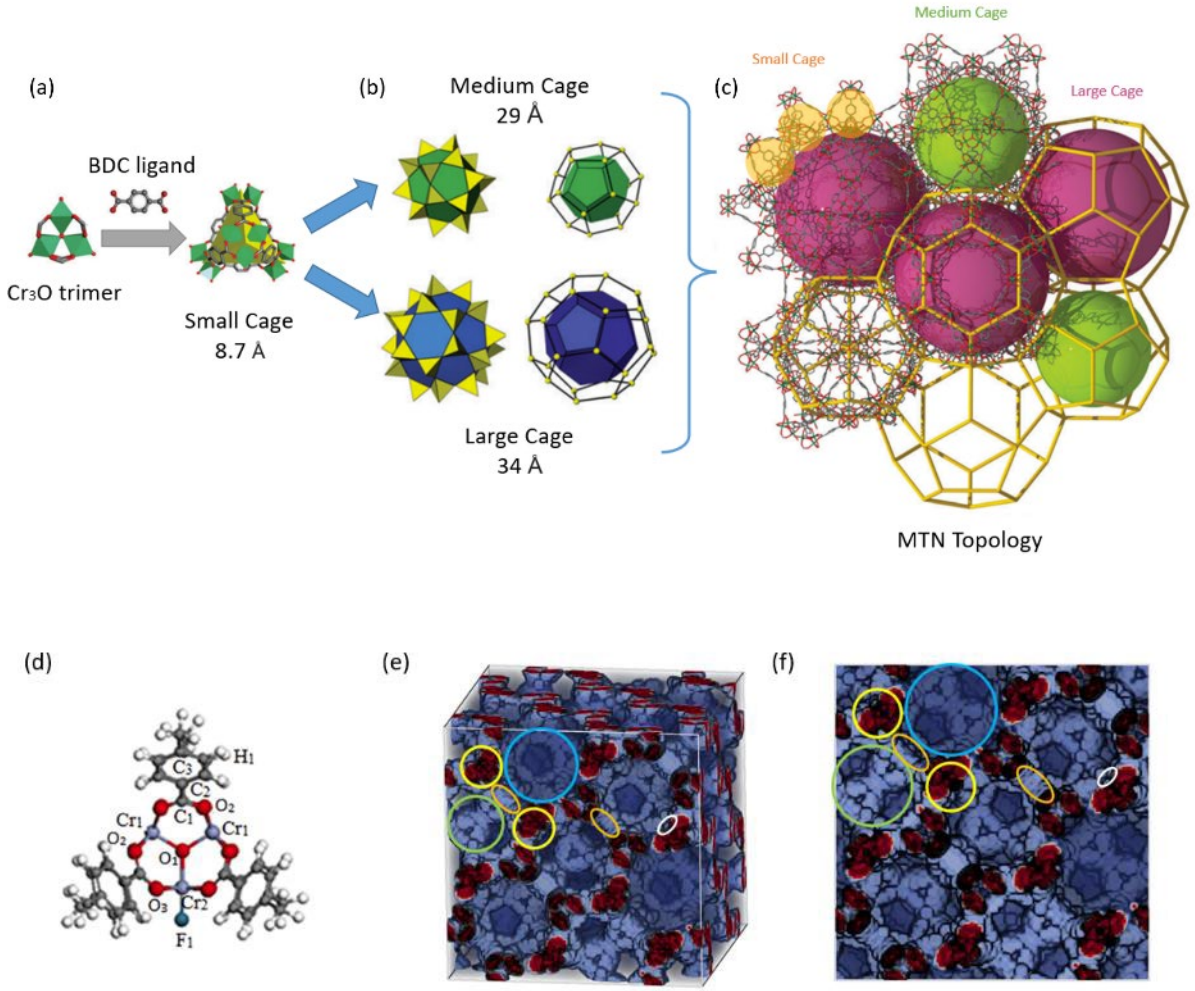

Figure 1. (a) Tetrahedral cage of MIL-101; (b) Medium and Large cage of MIL-101 [35]; (c) Topology of MIL-101 [36]; (d) Atom labels of MIL-101 [24]; (e) 3D view of Simulation Cell; (f) 2D view of Simulation Cell (Large cage: blue; Medium cage: green; Small cage: yellow; Pentagon window: orange; Triangle window: white).

To investigate the adsorption of CH_4 and N_2, and their mixture in MIL-101(Cr), the RASPA2 platform [37], a molecular simulation software program, was employed. The grand canonical Monte Carlo (GCMC) approach was utilized, where the adsorbate chemical potential, volume, and temperature were kept constant during the simulations. The structure of MIL-101(Cr) (https://github.com/iRASPA/RASPA2/blob/master/structures/mofs/cif/MIL-101.cif) depicted in Figure 1 was considered as rigid in these simulations. Within the simulation cell, CH_4 and

N_2 molecules were allowed to exhibit various forms of motion, including swapping, rotation, and translation. Lennard-Jones (L-J) potential functions were employed to model the van der Waals interactions between the CH_4 and N_2 molecules and the atoms of the MIL-101(Cr) framework [37].

$$U_{VDW} = 4\varepsilon_{ij}\left[\left(\frac{\sigma_{ij}}{r_{ij}}\right)^{12} - \left(\frac{\sigma_{ij}}{r_{ij}}\right)^{6}\right] \quad (1)$$

When σ_{ij} is the finite distance at which the inter-particle potential is zero, ε_{ij} is the depth of potential well, r_{ij} is the distance between the particles *i* and *j*, and the Lorentz–Berthelot rules can be used to determine the "strength" and "size" parameters that describe the potential as follows

$$\varepsilon_{ij} = \sqrt{\varepsilon_i \varepsilon_j}\,,\ \sigma_{ij} = \frac{1}{2}(\sigma_i + \sigma_j) \quad (2)$$

Coulombic interactions between charged particles were modeled via the Ewald approach [37].

$$U_{Coul}(r_{ij}) = \frac{q_i q_j}{4\pi\varepsilon_0 r_{ij}} \quad (3)$$

where ε_0 is the dielectric permittivity of vacuum and q_i and q_j are the respective partial charges of atoms *i* and *j*.

The GCMC method considers the chemical potential, volume, and temperature as independent variables within the μVT ensemble. In this ensemble, the chemical potential is held constant while the temperature and system volume are fixed. It is worth noting that the chemical potential is typically determined based on fugacity rather than pressure. Those GCMC calculations were conducted at a temperature of 298 K and a fixed pressure ranging from 0.1 to 1 bar. The L-J 12-6 potential calculation employed a cutoff radius of 12 Å. The Van der Waals interactions were computed using an atom-based summation approach, while the electrostatic interactions between the listed atoms were evaluated using the Ewald summation method. During the GCMC simulations, MIL-101(Cr) frameworks with 1×1×1 unit cells (88.869 × 88.869 × 88.869 $Å^3$) were utilized, and periodic boundary conditions were applied in all three dimensions. The equilibration phase involved the first 5,000 moves, and ensemble averages were computed using the final 25,000 steps. All simulations included random insertion/deletion, translation and rotation moves of molecules with equal relative probabilities,

which are properly normalized within the RASPA2 code. So they only need to be specified relative to each other [37]. Detailed information regarding the L-J potential parameters and atomic charges for each labeled atom can be found in Table 1. The CH_4 molecule was represented using a rigid five-site model[38], where partial charges and L-J potential parameters were assigned to both the C and H atoms to replicate their electrostatic characteristics and van der Waals interactions. The partial charges on the C and H atoms were derived from the calculation of the octopole moment. Specifically, the partial charge on each hydrogen atom q_H is 0.165e, and the partial charge on the carbon atom q_C is -0.66e, where e represents the magnitude of the electronic charge. The N_2 molecule was described by a rigid 3-site with partial charges located on the N and N_{com} atoms of N_2 to reproduce its electrostatic potential and a Lennard-Jones site located on the N atom [24]. The L-J parameters of the atoms in MIL-101 are all from the DREIDING [39] and UFF [40] force fields, and the partial charges of the atoms are all from the work of Du et. al [37]. To aid in comprehending the structural information (e.g. 3D topological view, 3D density distribution profile, volume visualization mode, atom visualization mode), we utilized iRASPA[41], a structural visualization tool that facilitated the visualization of the simulated results.

Table 1. L-J potential parameters and charges of CH_4 and N_2 and MIL-101(Cr) [24, 38-40, 42].

Molecule	**Unique identifier**	**Atom**	**L-J parameter**		**Charge / e**
			ε/k_B (K)	σ (Å)	
CH_4	CAS RN: 74-82-8	C_CH_4	55.055	3.40	-0.66
		H_CH_4	7.901	2.65	0.165
N_2	CAS RN: 7727-37-9	N_N_2	36.00	3.31	-0.48
		N_com[α]	-	-	0.96
MIL-101(Cr)	cif file name: MIL-101(Cr)	O1	48.16	3.03	-0.85
		O2	48.16	3.03	-0.57
		O3	48.16	3.03	-0.44
		C1 [24]	52.87	3.43	0.50
		C2 [24]	52.87	3.43	-0.07
		C3 [24]	52.87	3.43	-0.06
		H1 [24]	22.14	2.57	0.11
		F1 [42]	36.48	3.09	-0.55
		Cr1	7.55	2.69	1.62
		Cr2	7.55	2.69	1.35

[α] N_com represents massless virtual site, placed at the molecular center of mass.

2.2 Molecular Dynamics Simulations

To investigate the self-diffusion properties of guest molecules within MIL-101, we employed MD simulations using the LAMMPS software [43]. The simulations were conducted in both the canonical ensemble (NVT) and microcanonical ensemble (NVE) to examine the behavior of gas molecules within the different cavities of MIL-101(Cr). For those MD simulations, MIL-101 frameworks with 1×1×1 unit cells (88.869 × 88.869 × 88.869 $Å^3$) were utilized, and periodic boundary conditions were applied in all three dimensions. The L-J potential was employed to model the intermolecular interactions, with a cutoff radius of 12 Å. This is because cutoff radius for 12 Å is based on empirical experience of LAMMPS with the Leonard Jones interaction in the pair_style command [44] (e.g. pair_style lj/cut/coul/long 12). The parameters for the interaction between atoms of different species, which are not explicitly provided, were determined using the customary Lorentz-Bertelot combining rules (e.g. pair_modify mix arithmetic). The Particle-Particle Particle-Mesh (PPPM) summation approach was used to calculate the long-range electrostatic interactions with a precision of 1×10^{-4} (e.g. kspace_style pppm 0.0001). The tail correction [45] was used for computing the long-range interactions of certain pairs during the simulations (e.g. pair_modify tail yes). Newton's laws of motion were integrated into the equation of motion using the Velocity-Verlet technique. The simulation time step was set to 0.2 fs. Each MD simulation consisted of a total duration of 11 ns, with 10 ns allocated for equilibration and 1 ns for production to ensure a stable state and achieve complete statistical averaging [46, 47]. A Nose-Hoover thermostat with a damping coefficient of 100 time-steps at 300 K was employed to control the temperature. The MD simulations considered the flexibility of the MIL-101 framework but treated CH_4 and N_2 as rigid bodies. As shown in Table S3, the force field parameters for MIL-101(Cr) flexible framework were calculated from LAMMPS Interface[48]. Such approach has been widely utilized for MOFs with flexible frameworks [49].

3. Results and discussion

3.1 Adsorption of Pure CH_4 and N_2

3.1.1 Simulation Validation of Pure Gases

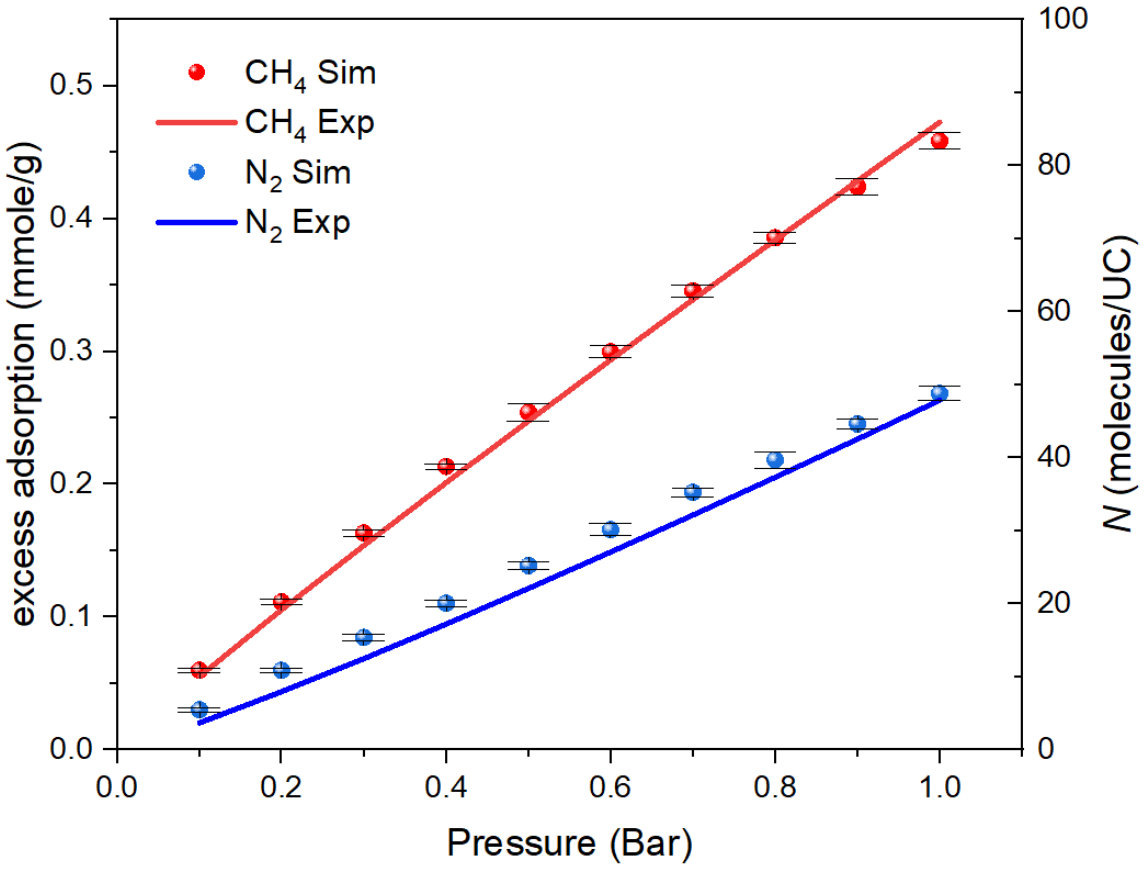

Figure 2. CH_4 [19] and N_2 [50] adsorption isotherms comparison of GCMC simulations and experimental measurements in MIL-101(Cr) at 298 K.

The simulated adsorption isotherms of CH_4 and N_2 on MIL-101(Cr) at 298 K were compared with experimental data to validate the simulation results [19, 50]. Figure 2 and Table S1 show that the simulated adsorption isotherms were slightly higher than the values obtained from the experimental data. This can be attributed to the absence of crystal defects or impurities in the MIL-101(Cr) model used in the simulations, which may have a minor influence on the adsorption capacity. Figure 2 also reveals that the adsorption capacity of both CH_4 and N_2 increases with increasing pressure. However, the rate of increase for CH_4 is noticeably higher than that for N_2. Additionally, the adsorption capacity of CH_4 is higher than that of N_2 under investigated conditions. It can be also obtained from Figure 2 and Table S1 that under the

pressure range of 0.1-1 bar, one unit cell of MIL-101(Cr) is capable of adsorbing between 11 and 86 CH_4 molecules, and between 6 and 50 N_2 molecules, respectively. These findings suggest that MIL-101 exhibits better adsorption performance for CH_4 compared to N_2, particularly at low pressures.

The isosteric heat of adsorption (Q_{st}) is a crucial parameter that reflects the strength of interaction between an adsorbent and an adsorbate, particularly at low pressures or low loading conditions. In this study, the Q_{st} values for CH_4 and N_2 adsorption on each MOF at different operating temperatures were estimated using the GCMC method. The calculation of Q_{st} was performed using Equation (4) as described in the literature [42].

$$Q_{st} = RT - \frac{\langle UN\rangle - \langle U\rangle\langle N\rangle}{\langle N^2\rangle - \langle N\rangle^2} \qquad (4)$$

Where U is the change in internal energy of intermolecular interactions in the adsorbed phase during the adsorption process, N is the molecular weight of the adsorption, R is the gas constant, and <> is the average value. The complete derivation process for Equation (4) can be found in the Supporting Information.

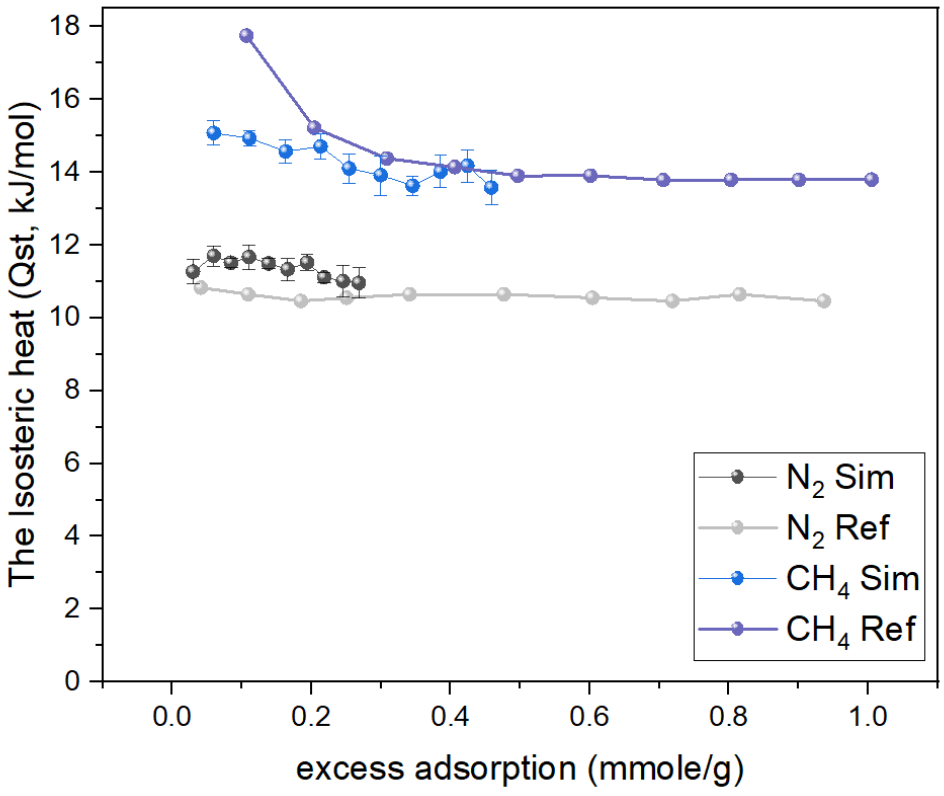

Figure 3. Isosteric heat of adsorption (Q_{st}) for N_2 [51] and CH_4 [52] in MIL-101.

The fluctuation of the isosteric heat of adsorption for CH_4 and N_2 on MIL-101 at 298 K is presented in Figure 3 and Table S2. The Q_{st} values for CH_4 are consistent with previous findings reported by Pradip et al. [52], who reported values of approximately 14-18 kJ/mol. However, it is important to note that at low loading, our simulation results indicate a value of around 15.08 kJ/mol, which deviates slightly from their findings (17.75 kJ/mol). As the loading increases, the enthalpy of adsorption for CH_4 shows a slight decrease, ranging from approximately 15.08 kJ/mo at 0.06 mmol/g to around 13.57 kJ/mol at 0.46 mmol/g. This observation can be attributed to the dominant role of van der Waals forces and electrostatic interactions in the low-load region, while in the high-load region, as the adsorption sites become saturated, the Q_{st} decreases.

For N_2, the simulation outcomes closely align with the experimental results reported by Zhang et al. [51]. The enthalpy of adsorption for N_2 exhibits only slight variations with loading. Notably, the Q_{st} values for CH_4 are significantly higher than those for N_2, indicating stronger interactions between CH_4 molecules and the MIL-101 framework. The accuracy and reliability of our simulation results for both the adsorption isotherms and Q_{st} values have been confirmed, thus validating the usage of the GCMC simulation method in the grand canonical ensemble for further research.

3.1.2 Radial Distribution Functions of Pure Gases

The RDF is mainly used for point-to-point quantitative research on which atoms in the adsorbent play a major role in gas adsorption, so as to know which adsorption sites in the adsorbent and which atoms the adsorption sites are composed of [53]. This function is to count the number of two-atom species at a given distribution distance, which can be specified as [49]:

$$g_{ij}(r) = \frac{<\Delta N_{ij}(r,r+\Delta r)>V}{4\pi r^2 \Delta r N_i N_j} \qquad (5)$$

where V is the system volume, N_i and N_j are the numbers of atoms i and j, respectively, and Δr is the distance between atoms i and j. $N_{ij}(r, r + r)$ is the number of atom j surrounding i within a shell from r to $r + \Delta r$.

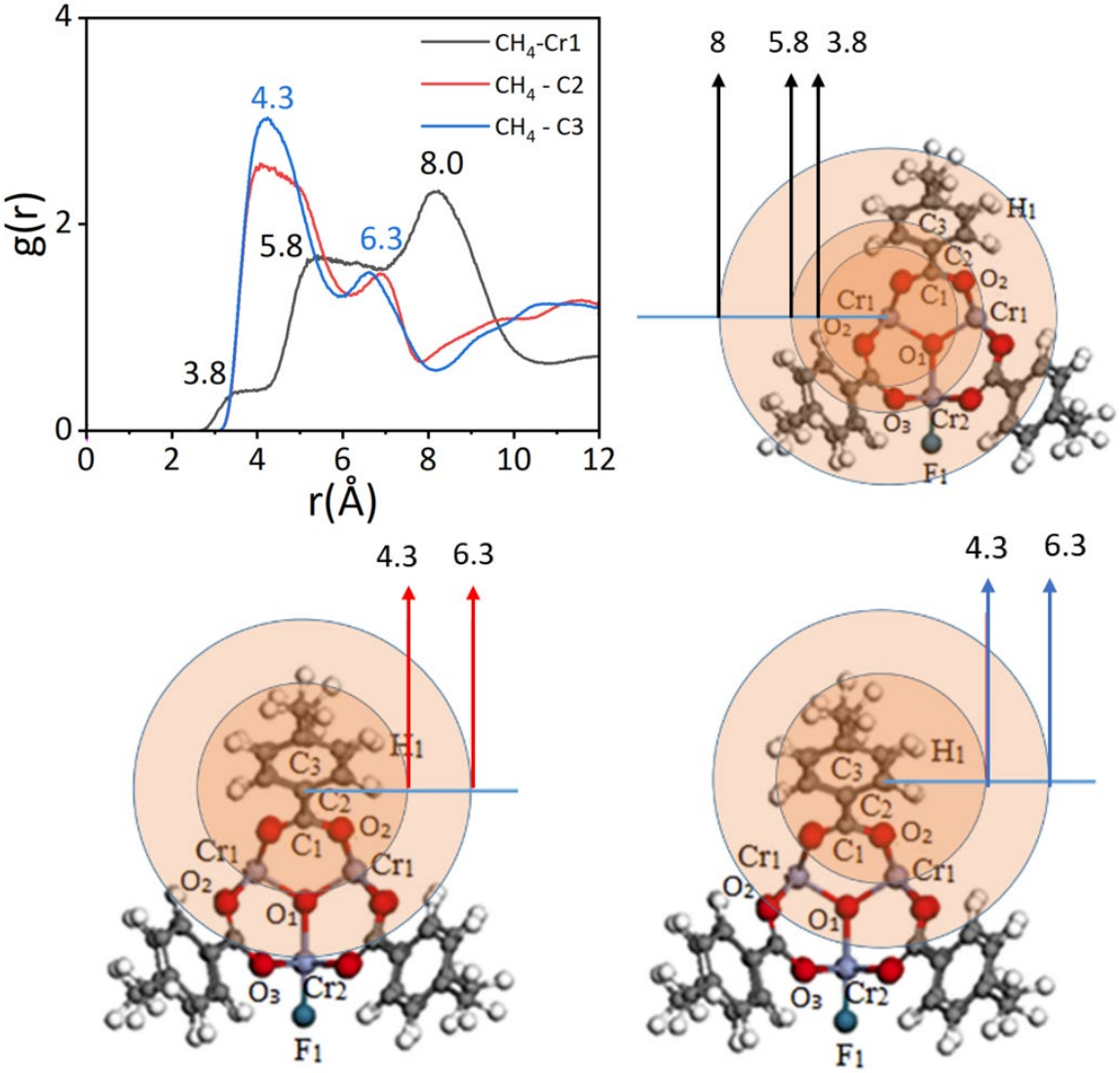

Figure 4. RDF of CH_4 around Cr1 atom and C3 atom.

In Figure 4, the RDF curve for Cr1 exhibits three distinct peaks at approximately 3.8 Å, 5.8 Å, and 8 Å. The highest peak, located at 8 Å, indicates that CH_4 molecules tend to accumulate at this distance from the Cr1 atom. This accumulation is primarily influenced by the presence of C2 and C3 (C=C) atoms at the 8 Å distance, which facilitate the interaction between CH_4 and the framework. On the other hand, the peak observed at 5.8 Å shows a lower density of CH_4 molecules compared to the peak at 8 Å. This can be attributed to the increased steric hindrance effect [54] near 5.8 Å, which hinders further interaction between CH_4 and the C2/C3 atoms. The presence of nearby atoms and their spatial arrangement influence the accessibility and binding of CH_4 molecules at this distance. Furthermore, the peak observed at 3.8 Å is the result of the synergistic effect of multiple atoms, including O2, O1, and Cr1, on the adsorption of CH_4 at

this distance. The combined influence of these atoms contributes to the favorable adsorption of CH_4 molecules at the 3.8 Å distance. These findings highlight the important role of the C=C double bond in MIL-101 and its effect on the adsorption of CH_4. The study conducted by Qin et al. [55] supports these observations, further emphasizing the significance of the C=C double bond in facilitating the adsorption of CH_4 in MIL-101.

In Figure 4, there are peaks observed around 4.3 Å and 6.3 Å in the C2 and C3 curves. The highest peak at approximately 4.3 Å indicates that the majority of CH_4 molecules are adsorbed near the C=C bond in the MIL-101 framework. This suggests that the C=C bond plays a crucial role in the adsorption of CH_4 molecules, as it provides favorable interaction sites. Additionally, a smaller peak is observed around 6.3 Å, which can be attributed to the interaction between the Cr and O atoms in the MIL-101 framework. This interaction contributes to a smaller amount of CH_4 being adsorbed at this distance. Furthermore, it is noteworthy that the peak at 4.3 Å in the C3 curve is higher than that in the C2 curve. This difference can be explained by considering the structural differences around the C2 and C3 atoms. CH_4 molecules surrounding the C3 atom experience less steric hindrance compared to those surrounding the C2 atom, allowing for a higher density of adsorbed CH_4 molecules at the 4.3 Å distance. These findings provide insights into the specific adsorption sites and the role of the C=C bond and Cr and O atoms in the adsorption of CH_4 molecules in MIL-101.

The RDF diagrams of CH_4 for different types of atoms, as shown in Figures S2a-d, provide strong evidence of the significant influence of the C=C double bond on the adsorption of CH_4. The presence of Cr and O atoms also contributes to the adsorption process. The variation in peak heights observed in the RDF diagrams can be attributed to two main factors. Firstly, the distance from the adsorption site plays a role, as different locations of atoms can result in variations in peak heights. Secondly, steric hindrance effects can weaken the van der Waals force, leading to variations in the strength of adsorption at different distances. These findings reinforce the importance of the C=C double bond in CH_4 adsorption, while also highlighting the involvement of Cr and O atoms in the overall adsorption mechanism.

There are also related studies of CH_4 adsorption on MOFs (e.g. ZIF-8, ZIF-76, ZIF-69, MIL-101(Cr)) that have reached similar conclusions, supporting our research results. For example, Pérez-Pellitero et al. [56] reported that based on their molecular simulation, preferential adsorption sites for CH_4 in ZIFs (e.g. ZIF-8, ZIF-76, ZIF-69) are located in specific regions

close to the organic imidazolate linker, and not on the metal atoms. This contrasts with the behavior of several MOFs in which the preferential ad-sorption site is not on the organic linker, but on the metal center. Additionally, Wu et al. [57] reported that using neutron powder diffraction and difference Fourier analysis, they experimentally determined that the primary methane adsorption sites are associated with the organic linkers in ZIF-8. Meanwhile, Zhang et al. [58] reported that at a low loading, CH_4 primarily occupies the adsorption site proximal to the C=C bond of 2-methylimidazolate. Therefore, their study showed that the organic linker in ZIF-8 is the most preferential adsorption site, rather than the metal cluster. Furthermore, Qin et al. [55] reported that through DFT calculation for the analysis of the adsorption site of MIL-101(Cr), these gases (e.g. CH_4, C_2H_6, C_3H_8) are not adsorbed on the open metal site, which attracts negative charged atoms while the H of alkanes are positively charged. Their DFT calculations showed that the C–H···π distances exhibit a discernible trend, shortening as the gas molecule increases in size. Taking the shortest C–H···π distances as an example, they range from 3.70 to 3.14 Å for MIL-101-Cr, 3.70 to 3.16 Å for MIL-101-Fe, and 3.52 to 2.97 Å for MIL-101-Fe-NH_2, respectively. Simultaneously, C–H···O distances either decrease or increase. These findings underscore the critical role of C–H···π interactions.

The RDF results of Cr, O, C, and F for N_2 in Figure S3 show similarities to their respective RDF spectra for CH_4. This suggests that the adsorption behavior of N_2 and CH_4 is influenced by similar atomic sites within the MIL-101 framework.

3.1.3 Density Distribution Profile of Pure Gases

The primary application of 2D and 3D density distribution contour is to study the spatial distribution of gases in an adsorbent, with a specific emphasis on the point-to-volume topological relationship. These plots offer a more intuitive visualization of how gases are distributed throughout various channels and pores within the adsorbent.

Figure 5 and 6 depict the 2D density distribution profile of N_2 and CH_4 in MIL-101 with different molecules number projected onto the xy plane of at 300 K, respectively. It can be seen from Figure 5 that when the number of CH_4 molecules is 100, CH_4 is mainly distributed in pentagonal windows and the large and medium cages. With the increase of the number of CH_4 molecules, the large and medium cages are gradually filled by CH_4 molecules, but as the number of CH_4 molecules reaches 800, few CH_4 molecules begin to appear in the small cages of the tetrahedron, and the large and medium cavities were almost covered with CH_4 molecules.

The place with the highest density of CH_4 is on the edges of the pentagonal window connecting the large and medium cages. This shows that CH_4 has a high probability of adsorption on the edge of the pentagonal window.

However, the N_2 density profile is obviously different from that of CH_4. It can be clearly seen from Figure 4 that when the number of N_2 molecules is 100, most of the N_2 molecules are relatively uniformly distributed on the edges of the pentagonal window and the small cages of the tetrahedron, and a small amount of N_2 molecules appear inside the tetrahedron. As the number of N_2 molecules increases, N_2 molecules are gradually distributed in large, medium and small pores, but they do not appear in the same distribution pattern as CH_4. Most of CH_4 gather in medium and large pores, and very few appear in small pores. Instead, the highest N_2 density occurs in small tetrahedral cavities. It illustrates that N_2 has a high probability of adsorption in small cages.

In order to better understand their adsorption mechanisms, the 3D density distribution profile can be seen which atoms the molecules of CH_4 and N_2 are adsorbing to. The distribution of N_2 molecules and CH_4 molecules in MIL-101 can be seen more clearly from Figure 7a.I and Figure 7b.I. The area circled by orange is the small cavity of the tetrahedron. It can be clearly seen that there are very few CH_4 molecules in the tetrahedral cavity, but there are many N_2 molecules in that. So it can be concluded that N_2 is more likely to be adsorbed in small cavities than CH_4.

It can be seen from Figure 7a.II that CH_4 molecules are mainly distributed on the edge of the pentagonal window rather than triangle window. As illustrated in Figure 7a.II, the highest concentration of CH_4 is found at the C=C double bond of the benzene ring, close to the C3 and C2 atoms. Few CH_4 molecules appear near the trimer of Cr and O atoms. The results observed by the 3d density distribution profile are basically consistent with the results analysed by the RDF spectrum. So it shows that C=C double bond and unsaturated metal (Cr) are the main adsorption sites of CH_4 molecules.

However, the 3d density distribution of N_2 is obviously different from that of CH_4. It can be seen from Figure 7b.II that N_2 molecules are mainly distributed near the tetrahedron (including the edge and body), and few is distributed on the edge of the pentagonal window. It is also observed that the main interactive atoms in MIL-101 are also near the C=C double bond on the benzene ring and the trimer of unsaturated metal (Cr).

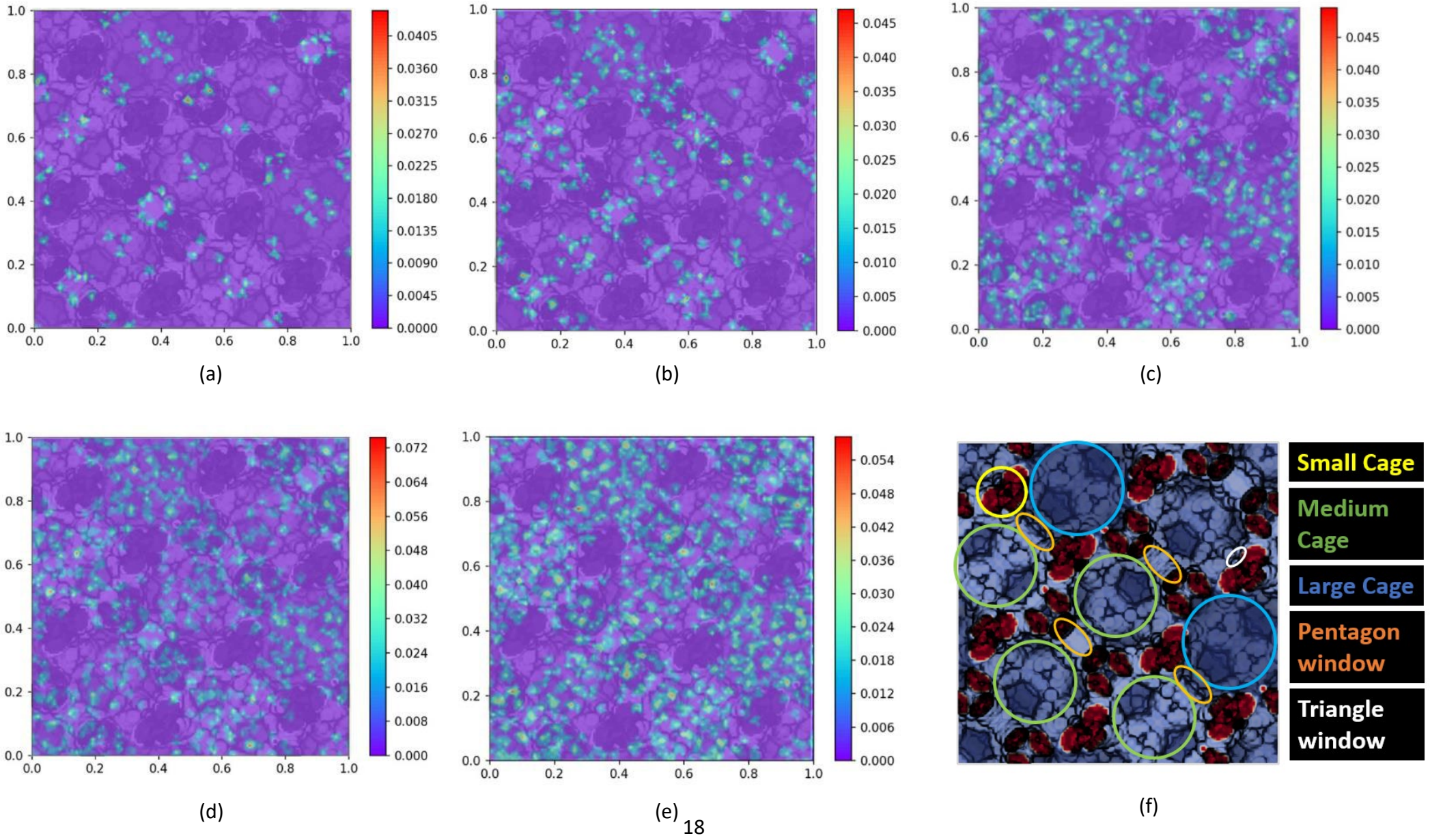

Figure 5. 2D Density distribution for CH_4 in MIL-101 with different numbers of CH_4 molecules. (a) Number = 100, (b) Number = 200, (c) Number = 400, (d) Number = 600, (e) Number = 800, (f) 2D view of Simulation Cell.

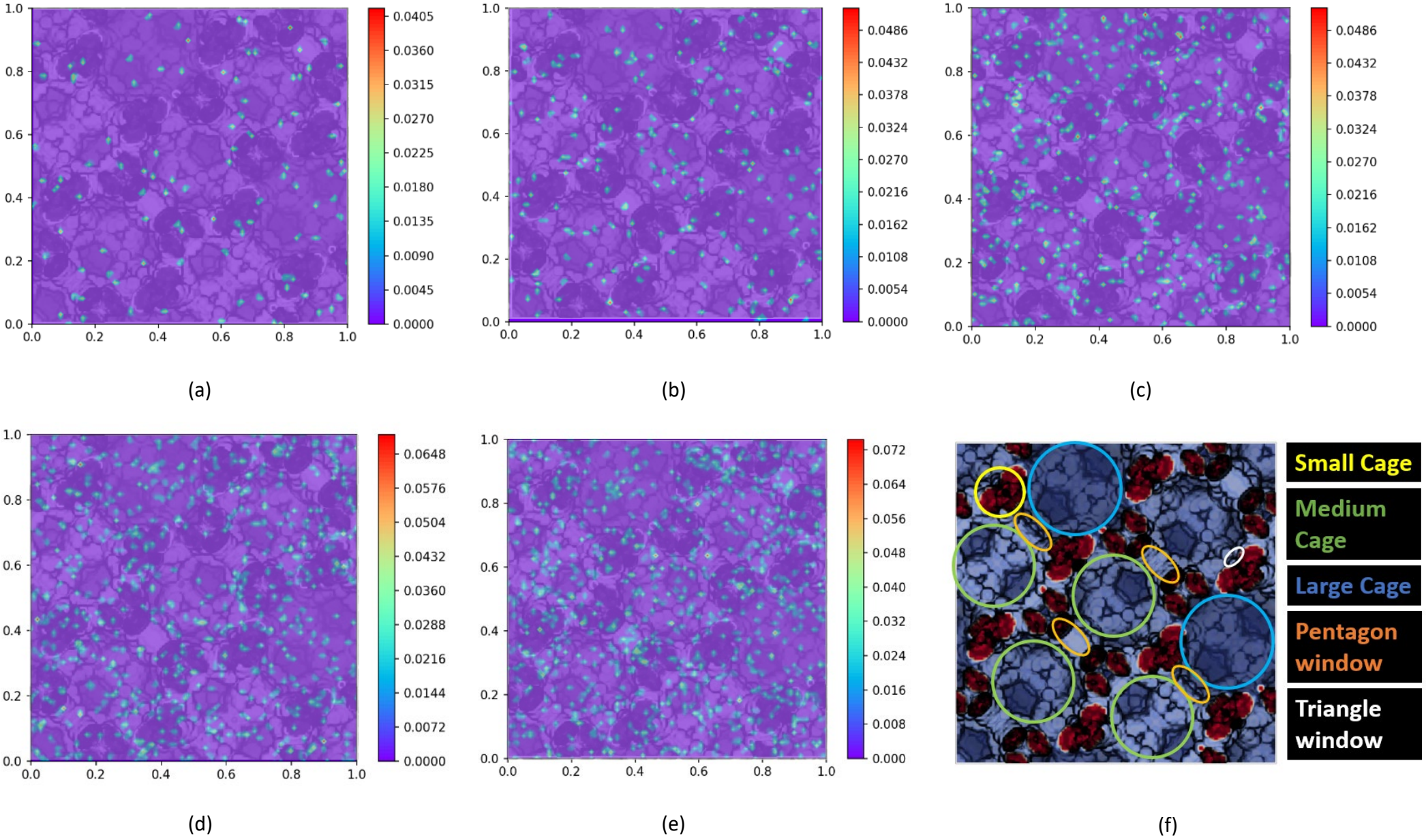

Figure 6. 2D Density distribution for N_2 in MIL-101 with different numbers of N_2 molecules. (a) Number = 100, (b) Number = 200, (c) Number = 400, (d) Number = 600, (e) Number = 800, (f) 2D view of Simulation Cell.

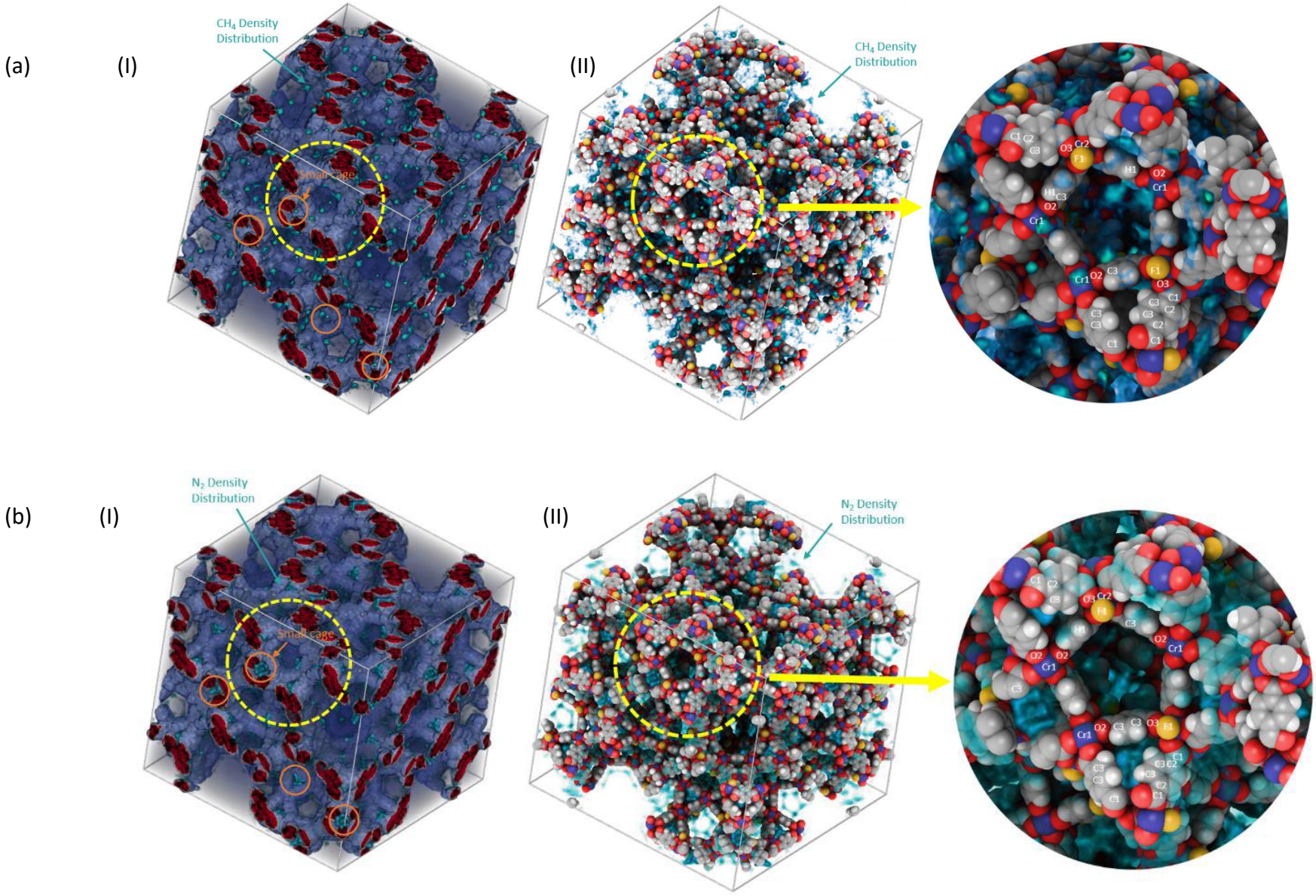

Figure 7. (a) 3D Density distribution for CH_4; (b) 3D Density distribution for N_2; (I) Volume visualization mode; (II) Atoms visualization mode.

Table 2. Pore windows and Pore diameter of MIL-101 calculated using HOLE Program [59].

Type	Diameter (Å)
Large Cage	32.0
Hexagonal Pore window	13.0
Medium Cage	28.0
Pentagonal pore window	10.0
Small Cage	6.6
Triangle pore window	4.8

The structure and availability of the pores in MIL-101 are currently being examined. Morphologies and channel diameters within the material have been calculated utilizing the HOLE program [59], as presented in Table 2. Figure S4 reveals a triangular pore window with a diameter of 4.8 Å, slightly larger than the kinetic diameter of CH_4 (3.8 Å). Due to the random movement of CH_4 molecules, the probability of them passing through such a small window is extremely low, making the triangular pore window inaccessible to CH_4. Conversely, N_2 with a diameter of 3.0 Å, 20% smaller than CH_4, has a higher probability of passing through the triangular pore window. The hexagonal and pentagonal pore windows, with diameters of 13.0 Å and 10.0 Å respectively, are much larger than the critical diameter of CH_4, allowing both CH_4 and N_2 to easily access the medium and large cages within MIL-101.

In summary, the density distribution profile indicates that N_2 can be evenly distributed throughout MIL-101, while CH_4 faces limitations due to the size difference between the molecules and the pore structure. N_2's smaller size enables it to pass through smaller pore windows, resulting in a more uniform distribution. The pore structure of MIL-101 and the size of gas molecules are key factors determining their distribution patterns within the material.

3.1.4 Self-Diffusion Coefficients and Diffusion Activation Energy of Pure Gases

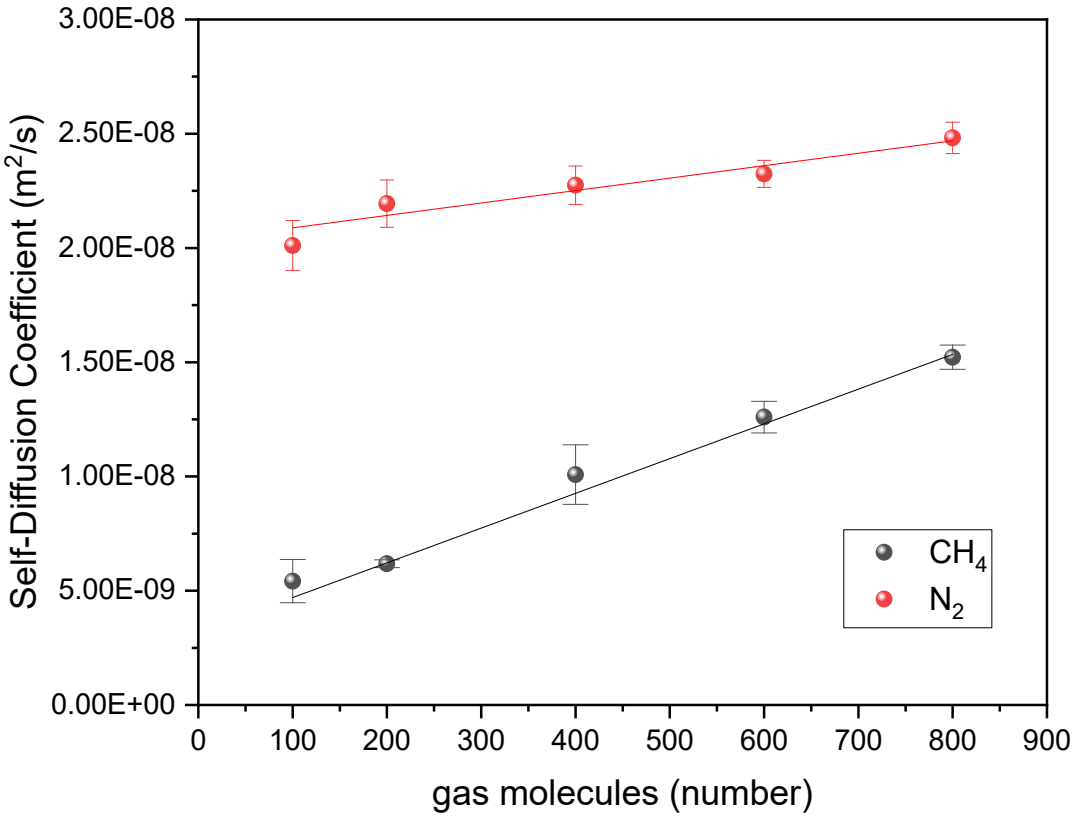

Figure 8. Self-diffusion coefficients of CH_4 and N_2 molecules in MIL-101(Cr).

The self-diffusion coefficient (D_s) serves as a quantitative tool for analysing adsorption kinetics. Its primary purpose is to compare the diffusion rates of different gases within an adsorbent, with a particular focus on the randomized Brownian motions of the gas itself influenced by the adsorbent [60]. This differs from the analysis conducted by RDF and density distribution functions, which primarily concentrate on examining the adsorption sites within the adsorbent.

The D_s of N_2 and CH_4 in MIL-101 at 298 K were investigated to understand their diffusion properties. The D_s values were determined by calculating the mean-squared displacement (MSD) of the molecules. The average MSD of molecule j, as described in Equation (6), is directly related to the diffusion coefficients according to the Einstein equation. By

analysing the MSD, we can obtain valuable insights into the diffusion behaviour of N_2 and CH_4 within MIL-101 at different loadings and concentrations [49].

$$D_{xyz}^{self} = \lim_{t\to\infty} \frac{1}{6t} \langle \frac{1}{N} \sum_{j=1}^{N} \| r_j(t) - r_j(0) \|^2 \rangle \qquad (6)$$

where N is the number of molecules j in the simulation system, $r(t)$ represents the position vector of molecule j at time t, and <…> denotes an ensemble average.

To calculate the self-diffusion coefficients of CH_4 and N_2 in MIL-101, a series of simulations were performed. The MIL-101 structure was equilibrated at 300 K through a 1 ns simulation in the NVT ensemble, followed by a 10 ns simulation in the NVE ensemble to obtain the relaxed crystal structure. This procedure was conducted once for each set of framework parameters. Afterwards, the desired number of CH_4 and N_2 molecules were loaded into the relaxed structure, and the system was further simulated for 10 ns in the NVT ensemble to reach equilibrium. Subsequently, a 1 ns production run was performed in the NVT ensemble.

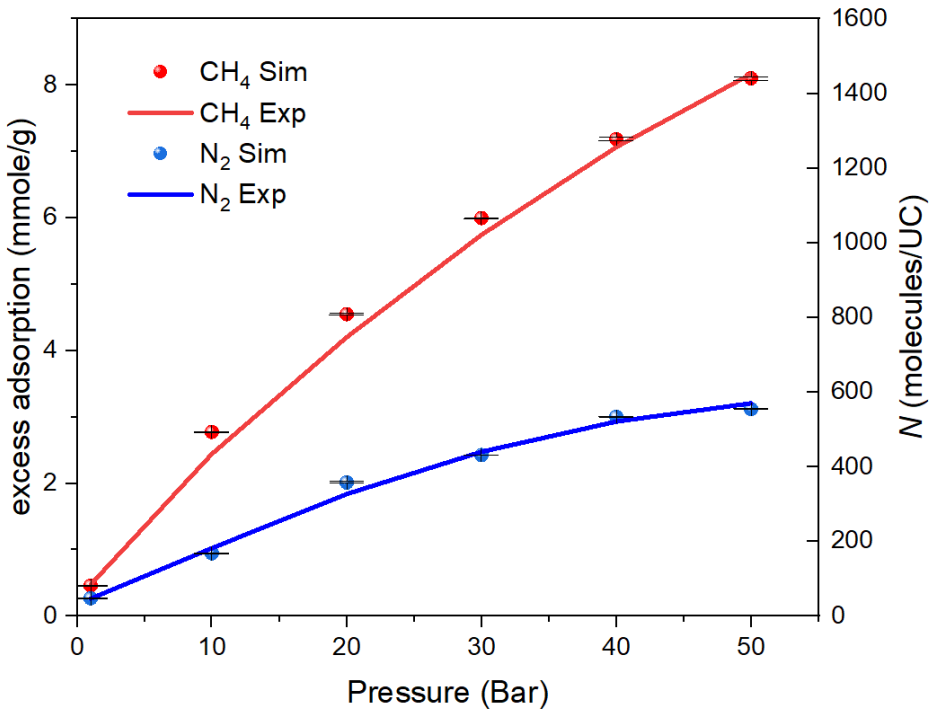

Figure 9. CH_4 [52] and N_2 [61] adsorption isotherms comparison of GCMC simulations and experimental measurements in MIL-101(Cr) at 298 K.

In Figure 8, we present a comparison of the self-diffusion coefficients of different numbers (e.g. 100, 200, 400, 600, 800) of CH_4 and N_2 molecules in MIL-101(Cr). The corresponding isotherm pressures of these numbers under GCMC simulations can be found in Figure 9 and Table S9. It can be also obtained that under the pressure range of 1-50 bar, one unit cell of MIL-101(Cr) is capable of adsorbing between 89 and 1524 CH_4 molecules, and between 50 and 582 N_2 molecules, respectively. The calculated self-diffusion coefficients fell within the range of 10^{-9} to 10^{-8} m^2/s, consistent with relevant studies by Sun et al. [62] on the experimental measurement of CH_4 gas diffusion coefficient (1.95 to 3.21 $\times 10^{-9}$ m^2/s) in porous materials, and Forse et al. [34] on the experimental study of the effect of pore size on the gas diffusion (1.5 to 6 $\times 10^{-9}$ m^2/s) in MOFs. Sedighi et al. [63] reported a study on the diffusion behavior of N_2 using modified MIL-101. Their study showed that the self-diffusion coefficient of N_2 is concentrated in the range of 2 to 6×10^{-8}. Additionally, Zhang et al. [58] used molecular simulation to examine adsorption and diffusion of CH_4 in ZIF-8. Their study showed that the value of the self-diffusion coefficient of CH_4 obtained from Zhang et al. is in the range of 10^{-10} to 10^{-9}. Figure 8 and Table S4 illustrate an increasing trend in the self-diffusion coefficients of both CH_4 and N_2, agreed well with previous work of Sedighi et al. [63] and Zhang et al. [58]. This can be attributed to the nearly constant number of adsorption sites in MIL-101, indicating that the atoms in MIL-101 exerting effective forces on CH_4 and N_2 remain unchanged. Consequently, when the number of CH_4 and N_2 molecules is low, the average force on each molecule is relatively higher, resulting in stronger binding and lower self-diffusion coefficients. Moreover, the self-diffusion coefficient of N_2 is higher than that of CH_4, indicating that N_2 exhibits easier diffusion, confirming that CH_4 is more readily adsorbed by MIL-101.

The impact of temperature on CH_4 and N_2 diffusion is depicted in Figure S5a, revealing a linear increase in self-diffusivity as temperature rises. This trend is consistent with similar observations in other microporous materials [64-65]. The enhanced movement of gas molecules at higher temperatures leads to an increase in their diffusion coefficients. Figure S5b presents the Arrhenius plots of CH_4 and N_2 diffusion parameters, there are many studies [66, 67, 68] using this method to get the activation energy of diffusion and commonly use to characterize gas diffusion in porous materials. According to the classical Arrhenius equation, the self-diffusion coefficient (D_s) can be calculated as $D_s = D_0 e^{-E_a/RT}$, where E_a is the activation energy of diffusion (kJ/mol), D_0 is the pre-exponential factor, R is the universal gas constant (8.314 J / mol·K), and T is the temperature (K). By plotting the inverse temperature ($1/T$) against the natural logarithm of the self-diffusion coefficient ($ln(D_s)$), the slope of the curve provides

information about the activation energy. Figure S5b demonstrates a good linear relationship (R^2 = 0.9701 and 0.9625) between $ln(D_s)$ and $1/T$, consistent with the equation $ln\,(D_s) = -\frac{E_a}{RT} + ln\,(D_0)$. The slope of the curve allows computation of the diffusion activation energies. In this case, the diffusion activation energies for CH_4 and N_2 in MIL-101 were determined to be 8.07 and 4.40 kJ/mol, respectively. A lower activation energy suggests a faster diffusion process with a smaller migration barrier to overcome. The higher activation energy for CH_4 compared to N_2 indicates that N_2 diffuses more easily than CH_4 in MIL-101.

3.2 Adsorption of CH_4 / N_2 Mixture

3.2.1 Simulation Validation of CH_4 / N_2 Binary Mixture

GCMC method is used to determined for the selectivity values of the CH_4/N_2 (0.3/0.7) [32] gas mixture in MIL-101 at 298 K and under various pressures. We set this ratio to the concentration ratio of the initial gas phase. The predicted selectivity values for the adsorption of CH_4 over N_2 for MIL-101 are shown in Figure. S8. The separation selectivity equation [26] is used to compute the data as shown below:

$$S_{1,2} = \frac{(x_1/x_2)}{(y_1/y_2)} \qquad (7)$$

where x and y, for components 1 and 2, denote the equilibrium adsorbed and gas phase mole fractions, respectively. A follow-up study on the adsorption of the adsorbent MIL-101 for the mixed two-component gas (CH_4 and N_2) behavior and adsorption mechanism, as well as adsorption sites, is needed to validate the simulated value with the experimental value of selectivity in order to increase the simulation's credibility [32]. It can be seen from Figure 10 and Table S8 that the simulated results are very close to the experimental values, and the simulated values are slightly higher than the experimental values. The main reason is that simulations have traditionally emphasized "ideal" crystals, but actual samples inevitably exhibit imperfections, ranging from minor defects to the interpenetration and localized collapse of the structure.

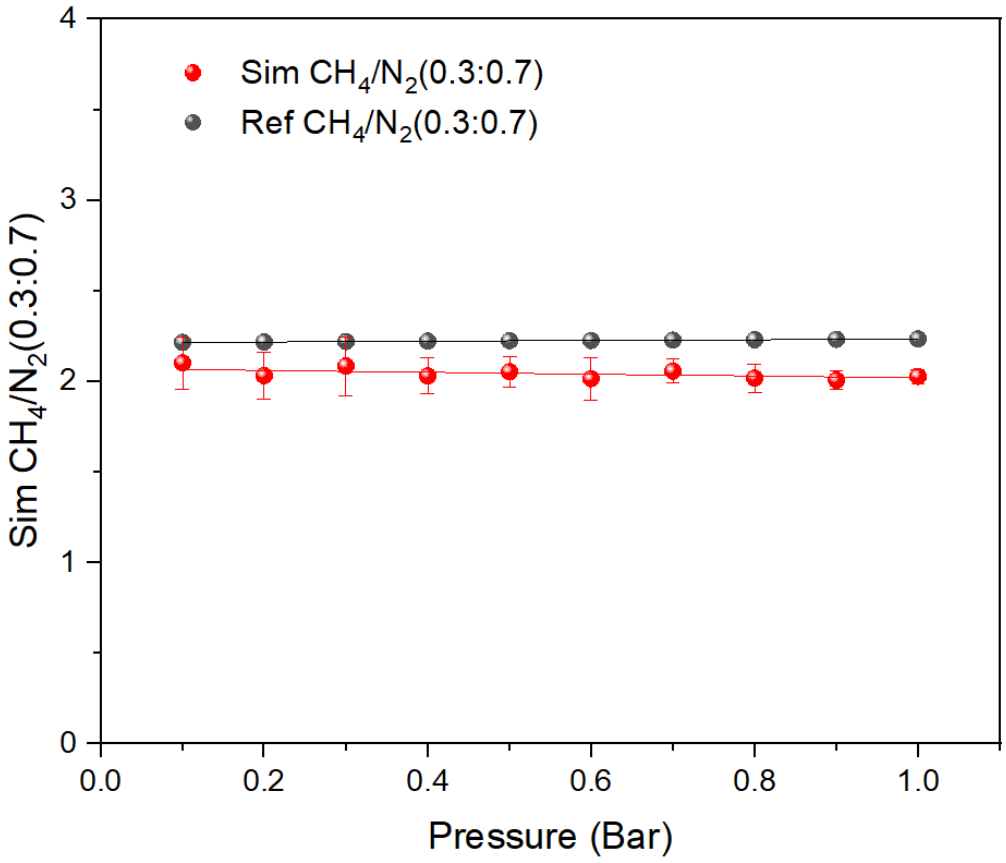

Figure 10. Separation selectivity values of CH_4/N_2 (0.3:0.7) mixture for the adsorption on MIL-101(Cr) at 298 K.

3.2.2 Density Distribution Profiles and Snapshot of CH_4/N_2 Binary Mixtures

Figure 11 illustrates the 2D density distribution profiles of CH_4 with varying numbers of N_2 molecules within MIL-101. In Figure 11a, it can be observed that the 200 CH_4 molecules are primarily distributed in the large and medium-sized cages, with some molecules also located near the pentagonal window. Notably, certain regions within the adsorbent exhibit clustering of CH_4 molecules. On the other hand, the 20 N_2 molecules tend to be concentrated near the small tetrahedral cavities and triangular windows, as depicted in Figure 11a.

Figures 11b to 11e demonstrate that, as the number of N_2 molecules increases, the overall distribution of CH_4 molecules remains largely unaffected. The previous distribution pattern is

maintained, and there is no apparent similarity between the distribution patterns of N_2 and CH_4. With the addition of more N_2 molecules, N_2 tends to exhibit a more even distribution throughout the adsorbent, without significant aggregation within individual cages. The highest density of N_2 molecules appears near the tetrahedron. Conversely, CH_4 molecules maintain their distribution pattern without a pronounced influence from the increasing number of N_2 molecules.

Furthermore, Figure 11 reveals that the highest density values of CH_4 increase as the number of N_2 molecules increases. This can be attributed to the fact that, when the overall number of CH_4 molecules remains constant, the introduction of more N_2 molecules leads to partial compression of CH_4 molecules, resulting in an increase in the highest density of CH_4 molecules. Simultaneously, the highest density of N_2 also exhibits an increment in response to the growing number of N_2 molecules, corresponding to the overall increase in the total N_2 molecule count.

Figure 12 depicts a snapshot of the distribution of 200 CH_4 molecules and different numbers of N_2 molecules in the adsorbent MIL-101. Through the display of 3D snapshots, the distribution of gas molecules can be seen more intuitively. As the increase of N_2 molecules does not affect the distribution of CH_4 molecules, it can be clearly seen that CH_4 molecules are agglomerated in large and medium-sized cages, and it can be clearly seen that N_2 molecules tend to distribute on the edges of large and medium-sized cages and windows, and also appear in the small cavity.

(a)

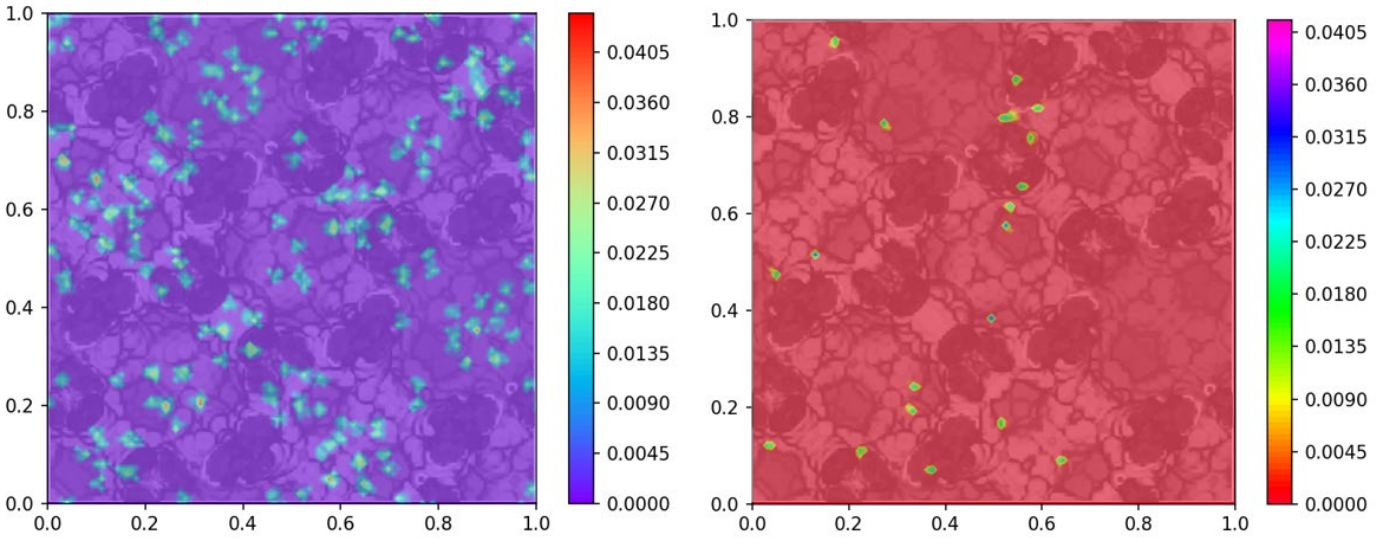
200 CH4 density profile
20 N2 density profile

(b)

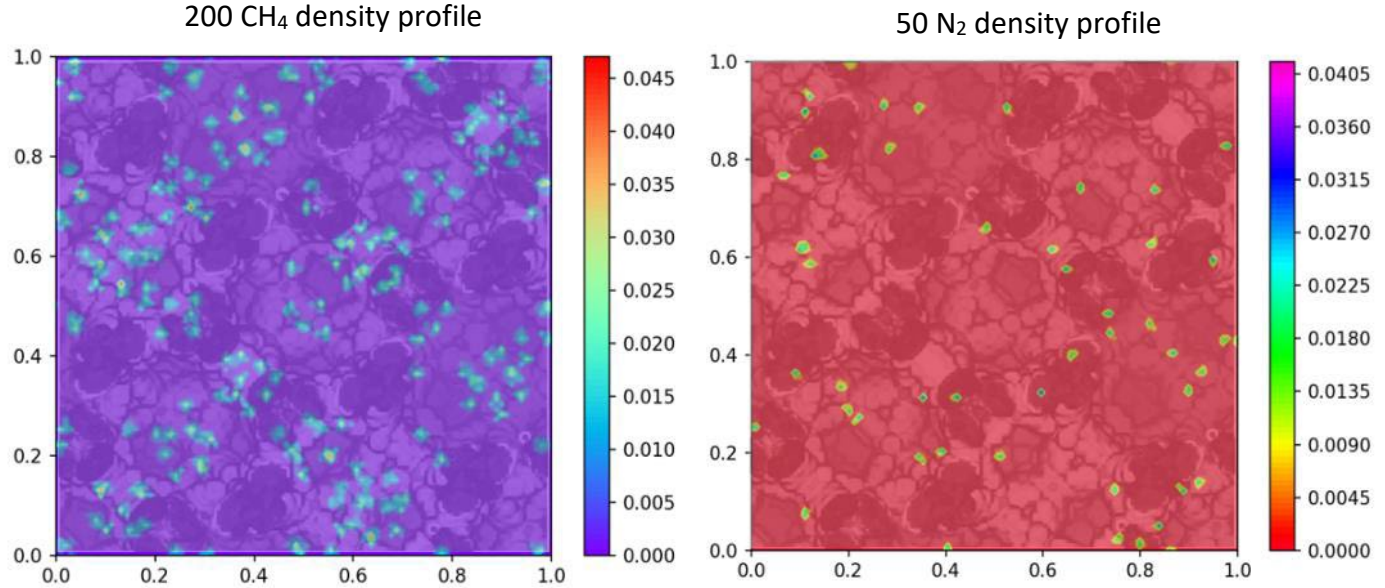
200 CH4 density profile
50 N2 density profile

(c)

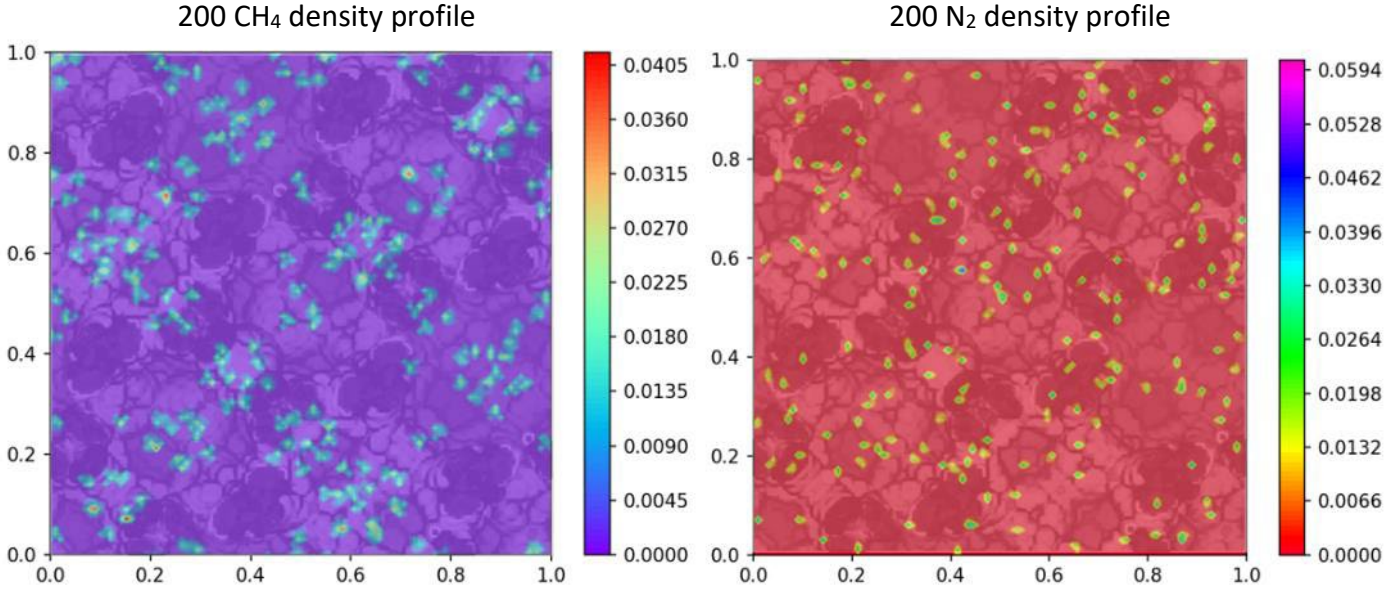
200 CH4 density profile
200 N2 density profile

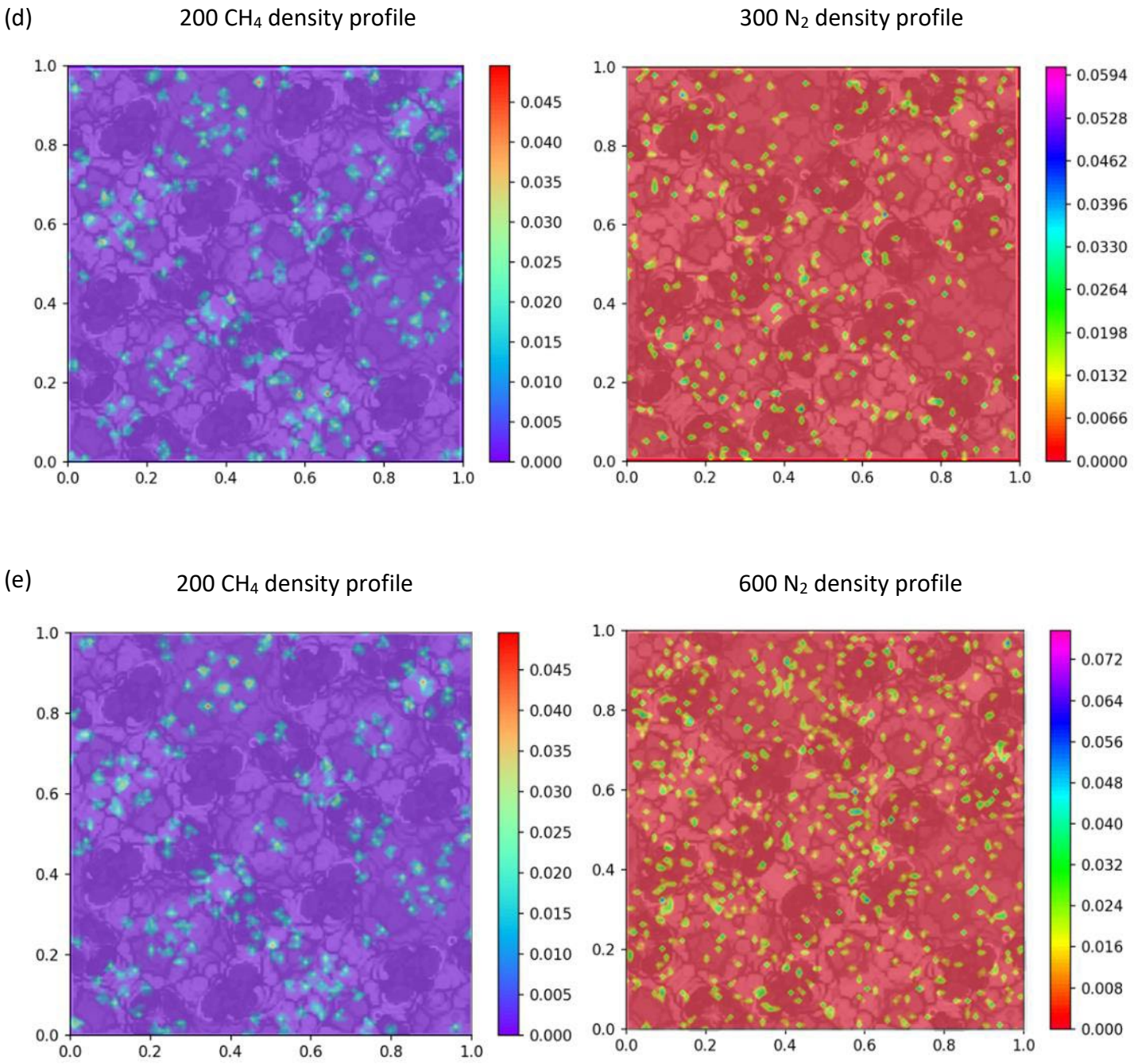

Figure 11. 2D Density distribution of CH_4 and N_2 for 200 CH_4 molecules in MIL-101 with different numbers of N_2 molecules. (a) Number = 20, (b) Number = 50, (c) Number = 200, (d) Number = 300, (e) Number = 600.

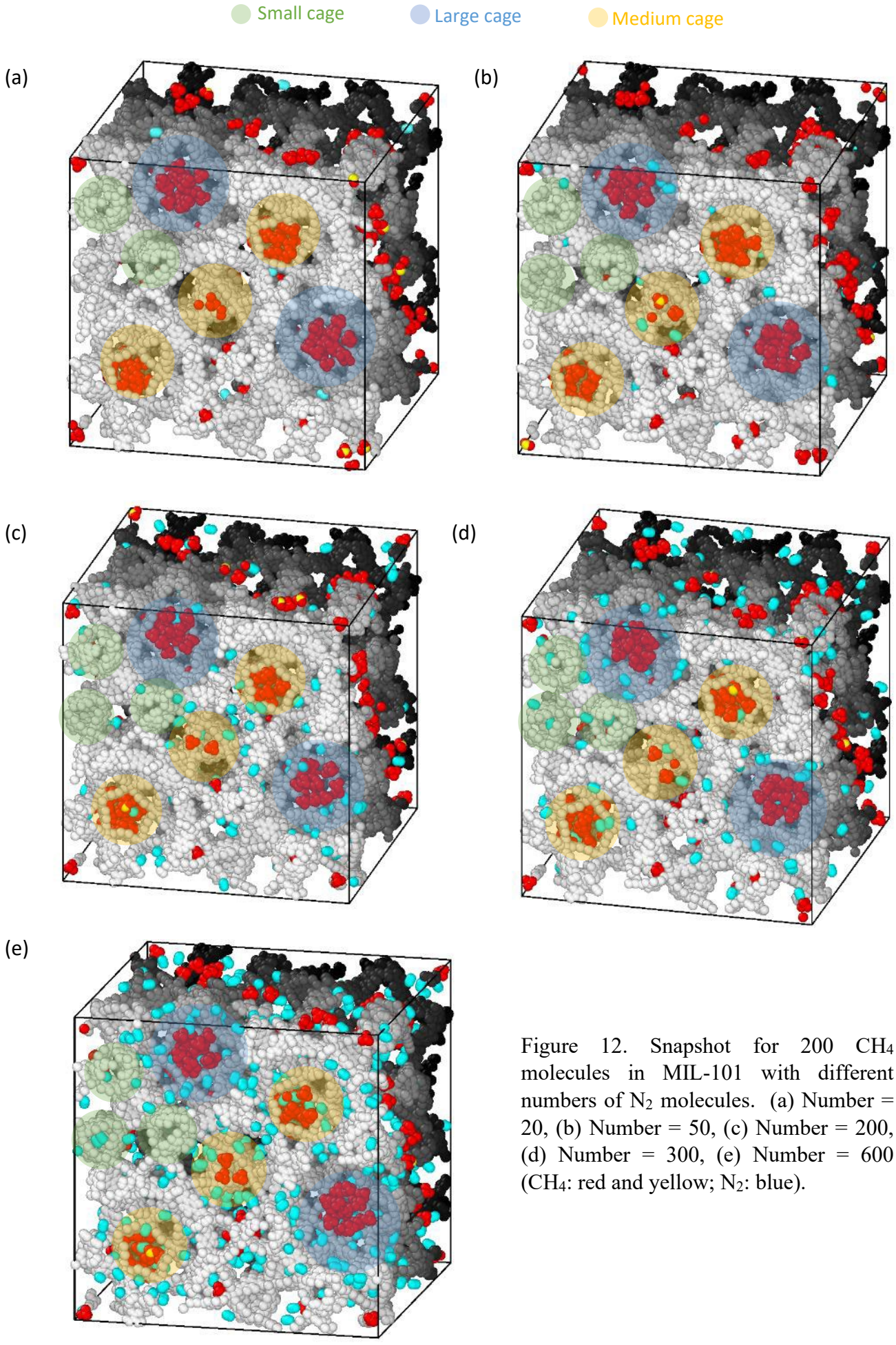

Figure 12. Snapshot for 200 CH_4 molecules in MIL-101 with different numbers of N_2 molecules. (a) Number = 20, (b) Number = 50, (c) Number = 200, (d) Number = 300, (e) Number = 600 (CH_4: red and yellow; N_2: blue).

3.2.4 Self-Diffusion Coefficients of CH_4/N_2 Binary Mixture

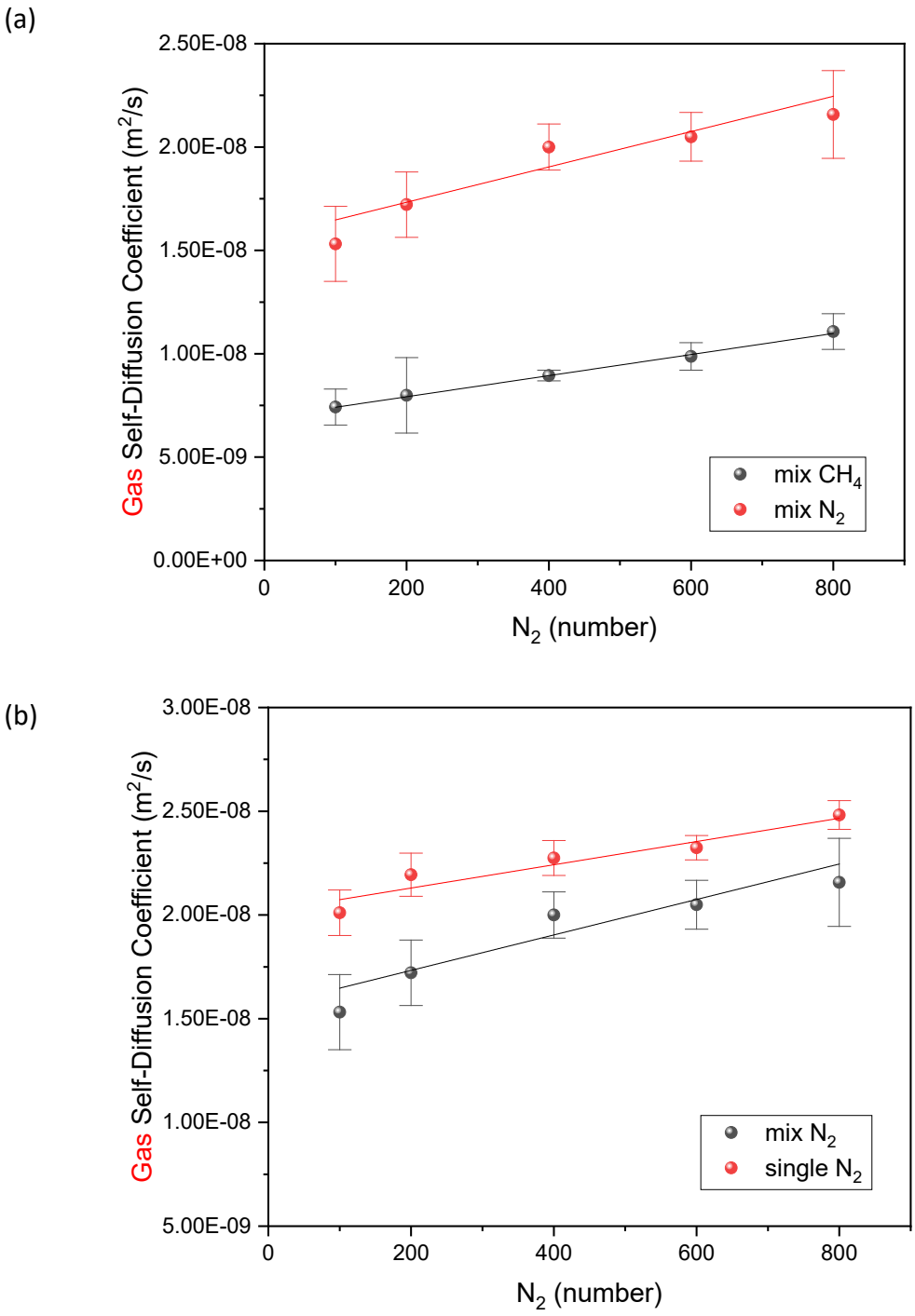

Figure 13. (a) Self-diffusion coefficients of CH_4 and N_2 when loading 200 CH_4 molecules in MIL-101 at different loadings of N_2 molecules at 298 K; (b) Self-diffusion coefficients of N_2 when compared loading 0 CH_4 molecules with 200 CH_4 molecules at different loadings of N_2 molecules at 298 K.

Figure 13a and Table S6 present the impact of increasing the number of N_2 molecules on the self-diffusion coefficient of each component in the binary mixture system of CH_4 and N_2. As depicted in the Figure 13a, the self-diffusion coefficients of N_2 and CH_4 exhibit a corresponding increase as the number of N_2 molecules increases in the binary gas mixture system. This behavior can be attributed to the fact that the total number of adsorption sites of the adsorbent is constant, and the increase in the number of gas molecules in the system will occupy more adsorption sites, the resulting reduction in the force exerted by the adsorbent on the newly added gas molecules leads to an increase in the diffusion coefficient. It is also worth noting that the self-diffusion coefficient of N_2 is higher than that of CH_4. This discrepancy arises from the higher selectivity of MIL-101 for CH_4 compared to N_2. The adsorbent exhibits a preference for adsorbing CH_4 molecules, leading to a greater occupation of adsorption sites by CH_4. Consequently, the Van der Waals and Coulomb forces exerted by the adsorbent on N_2 are diminished, resulting in a relatively higher self-diffusion coefficient for N_2.

Additionally, we conducted a comparison between the self-diffusion coefficient of N_2 in the absence of CH_4 molecules and in the presence of 200 CH_4 molecules, as shown in Figure 13b and Table S7. It is evident that with an increase in the number of N_2 molecules, both the self-diffusion coefficients of N_2 with and without CH_4 molecules increase. This can be attributed to a limited number of available adsorption sites for the newly introduced gas molecules.

The Figure 13b also shows that the self-diffusion coefficient of N_2 in the presence of 200 CH_4 gas molecules is significantly lower than that of pure N_2. When the concentration of N_2 is low, CH_4 exerts a greater hindrance on N_2 diffusion. However, as the concentration of N_2 increases, the difference between the self-diffusion coefficient of N_2 in the mixed gas and that in the pure gas diminishes. This reduction in difference is primarily due to the decreasing proportion of CH_4 in the mixture, leading to a reduced hindrance effect on N_2 diffusion. Such hinderance effect has been observed in many studies of CO_2/CH_4 [69], CO_2/N_2 [70], CO_2/Ar [71] and CH_4/N_2 [71] in porous materials. Therefore, we can conclude that in MIL-101(Cr), the presence of CH_4 assists in reducing the self-diffusion of N_2.

4. Conclusions

This study employs GCMC and MD simulations to investigate the adsorption and diffusion behavior of CH_4, N_2, and their mixture in MIL-101(Cr) adsorbent. Several properties were

computed and examined, including adsorption isotherms at varying temperatures, self-diffusion coefficients, isosteric heat of adsorption, density distribution profiles, radial distribution functions, and CH_4/N_2 selectivity values within the MIL-101 framework.

The results were consistent with anticipated outcomes.

1) The calculations of self-diffusion coefficient and isosteric heat of adsorption indicate that N_2 exhibits a higher self-diffusion coefficient compared to CH_4, suggesting that N_2 diffuses more easily. Moreover, both gases display a linear increase in self-diffusion coefficients with temperature. The diffusion activation energy calculations confirm that N_2 has a lower diffusion activation energy than CH_4, indicating its greater ease of diffusion. These results shed light on the transport properties of CH_4 and N_2 within the MIL-101 framework. 2) The CH_4/N_2 selectivity calculations align well with experimental data, underscoring the adsorbent's preference for CH_4 molecules. Additionally, the analysis of 2D density distribution profiles for binary mixtures reveals that the overall distribution of CH_4 molecules remains largely unaffected by an increase in the number of N_2 molecules.

In addition to the anticipated outcomes, the following summarizes the novel and original findings.

The RDF analysis reveals that the C=C double bond in MIL-101 is crucial for the adsorption of CH_4 and N_2, while the Cr and O atoms contribute to a lesser extent. Examination of the 2D density distribution profiles shows that CH_4 molecules preferentially occupy pentagonal windows, large and medium cages, with the highest density observed at the edges of the pentagonal window connecting the large and medium cages. Similarly, N_2 molecules exhibit a relatively uniform distribution along the edges of pentagonal and triangular windows, as well as in the small cages of the tetrahedron.

The 3D density distribution analysis highlights that the main interactive atoms in MIL-101 are located near the C=C double bond on the benzene ring and the trimer of unsaturated metal (Cr). These insights provide valuable information about the dominant adsorption sites and molecular arrangements within the adsorbent. The isosteric heat of adsorption is determined to be approximately 14 kJ/mol for CH_4 and 11 kJ/mol for N_2, respectively, indicating differing adsorption strengths for the two gases.

In the CH_4/N_2 selectivity analysis, the presence of CH_4 affects the N_2 diffusion trajectory, resulting in a smaller self-diffusion coefficient of N_2 in the mixed gas than that of single-

component N_2. Moreover, the introduction of more N_2 molecules causes some CH_4 molecules to be compressed together, leading to a change in the highest density value of CH_4.

These findings lay the groundwork for potential modifications aimed at enhancing the adsorption and selectivity properties of MIL-101 for the selective capture of coal-mine methane. The molecular simulation approaches employed in this study provide a precise understanding of the adsorption and desorption mechanisms within the MIL-101 framework.

Acknowledgement

This research was supported by the European Commission H2020 Marie S Curie Research and Innovation Staff Exchange (RISE) award (Grant No. 871998), and the 2023-24 SJTU-UoE Joint Seed Fund.

References

(1) Xu, H. Facilitating full and effective implementation of the Paris Agreement for carbon neutrality vision. *Carbon Neutrality* **2022**, *1* (1), 3.

(2) Gielen, D.; Kram, T. The Role of Non-CO 2 Greenhouse Gases in Meeting Kyoto Targets 1. 1998.

(3) Niu, Z.; Cui, X.; Pham, T.; Lan, P. C.; Xing, H.; Forrest, K. A.; Wojtas, L.; Space, B.; Ma, S. A Metal–Organic Framework Based Methane Nano-trap for the Capture of Coal-Mine Methane. *Angew. Chem. Int. Ed.* **2019**, *58* (30), 10138-10141.

(4) Ivanova, S.; Vesnina, A.; Fotina, N.; Prosekov, A. An Overview of Carbon Footprint of Coal Mining to Curtail Greenhouse Gas Emissions. *Sustainability* **2022**, *14* (22), 15135.

(5) Wang, X.; Zhou, F.; Ling, Y.; Xiao, Y.; Ma, B.; Ma, X.; Yu, S.; Liu, H.; Wei, K.; Kang, J. Overview and Outlook on Utilization Technologies of Low-Concentration Coal Mine Methane. *Energy & Fuels* **2021**, *35* (19), 15398-15423.

(6) Gulbalkan, H. C.; Haslak, Z. P.; Altintas, C.; Uzun, A.; Keskin, S. Assessing CH4/N2 separation potential of MOFs, COFs, IL/MOF, MOF/Polymer, and COF/Polymer composites. *Chem. Eng. J.* **2022**, *428*, 131239.

(7) Lv, D.; Wu, Y.; Chen, J.; Tu, Y.; Yuan, Y.; Wu, H.; Chen, Y.; Liu, B.; Xi, H.; Li, Z.; et al. Improving CH4/N2 selectivity within isomeric Al-based MOFs for the highly selective capture of coal-mine methane. *AlChE J.* **2020**, *66* (9), e16287.

(8) He, T.; Liu, Z.; Son, H.; Gundersen, T.; Lin, W. Comparative analysis of cryogenic distillation and chemical absorption for carbon capture in integrated natural gas liquefaction processes. *J. Clean. Prod.* **2023**, *383*, 135264.

(9) Nandanwar, S. U.; Corbin, D. R.; Shiflett, M. B. A Review of Porous Adsorbents for the Separation of Nitrogen from Natural Gas. *Ind. Eng. Chem. Res.* **2020**, *59* (30), 13355-13369.

(10) Zhang, J.; Li, L.; Qin, Q. Effects of micropore structure of activated carbons on the CH4/N2 adsorption separation and the enrichment of coal-bed methane. *Clean Energy* **2021**, *5* (2), 329-338.

(11) Mofarahi, M.; Bakhtyari, A. Experimental Investigation and Thermodynamic Modeling of CH4/N2 Adsorption on Zeolite 13X. *J. Chem. Eng. Data* **2015**, *60* (3), 683-696.

(12) Li, S.; Chen, J.; Wang, Y.; Li, K.; Li, K.; Guo, W.; Zhang, X.; Liu, J.; Tang, X.; Yang, J.; et al. Adsorption and separation of CH4/N2 by electrically neutral skeleton AlPO molecular sieves. *Sep. Purif. Technol.* **2022**, *286*, 120497.

(13) Jiang, C.; Wang, X.; Ouyang, Y.; Lu, K.; Jiang, W.; Xu, H.; Wei, X.; Wang, Z.; Dai, F.; Sun, D. Recent advances in metal–organic frameworks for gas adsorption/separation. *Nanoscale Advances* **2022**, *4* (9), 2077-2089, 10.1039/D2NA00061J.

(14) Liu, B.; Smit, B. Molecular Simulation Studies of Separation of CO2/N2, CO2/CH4, and CH4/N2 by ZIFs. *J Phys Chem C* **2010**, *114* (18), 8515-8522.

(15) Chang, M.; Zhao, Y.; Yang, Q.; Liu, D. Microporous Metal–Organic Frameworks with Hydrophilic and Hydrophobic Pores for Efficient Separation of CH4/N2 Mixture. *ACS Omega* **2019**, *4* (11), 14511-14516.

(16) Demir, H.; Keskin, S. Zr-MOFs for CF4/CH4, CH4/H2, and CH4/N2 separation: towards the goal of discovering stable and effective adsorbents. *Mol. Syst. Des. Eng.* **2021**, *6* (8), 627-642, 10.1039/D1ME00060H.

(17) Zorainy, M. Y.; Gar Alalm, M.; Kaliaguine, S.; Boffito, D. C. Revisiting the MIL-101 metal–organic framework: design, synthesis, modifications, advances, and recent applications. *Journal of Materials Chemistry A* **2021**, *9* (39), 22159-22217, 10.1039/D1TA06238G.

(18) Li, P.; Chen, J.; Feng, W.; Wang, X. Adsorption separation of CO2 and N2 on MIL-101 metal-organic framework and activated carbon. *J. Iran. Chem. Soc. J IRAN CHEM SOC* **2014**, *11* (3), 741-749.

(19) Liang, Z.; Marshall, M.; Ng, C. H.; Chaffee, A. L. Comparison of Conventional and HF-Free-Synthesized MIL-101 for CO2 Adsorption Separation and Their Water Stabilities. *Energy & Fuels* **2013**, *27* (12), 7612-7618.

(20) Zhang, F.; Shang, H.; Wang, L.; Ma, L.; Li, K.; Zhang, Y.; Yang, J.; Li, L.; Li, J. Substituent-Induced Electron-Transfer Strategy for Selective Adsorption of N2 in MIL-101(Cr)-X Metal–Organic Frameworks. *ACS Appl. Mater. Interfaces* **2022**, *14* (1), 2146-2154.

(21) Serra-Crespo, P.; Ramos-Fernandez, E. V.; Gascon, J.; Kapteijn, F. Synthesis and Characterization of an Amino Functionalized MIL-101(Al): Separation and Catalytic Properties. *Chemistry of Materials* **2011**, *23* (10), 2565-2572.

(22) Han, G.; Rodriguez, K. M.; Qian, Q.; Smith, Z. P. Acid-Modulated Synthesis of High Surface Area Amine-Functionalized MIL-101(Cr) Nanoparticles for CO2 Separations. *Industrial & Engineering Chemistry Research* **2020**, *59* (40), 18139-18150.

(23) Mahdipoor, H. R.; Halladj, R.; Ganji Babakhani, E.; Amjad-Iranagh, S.; Sadeghzadeh Ahari, J. Adsorption of CO2, N2 and CH4 on a Fe-based metal organic framework, MIL-101(Fe)-NH2. *Colloids and Surfaces A: Physicochemical and Engineering Aspects* **2021**, *619*, 126554.

(24) Sedighi, M.; Talaie, M. R.; Sabzyan, H.; Aghamiri, S.; Chen, P. Evaluating equilibrium and kinetics of CO2 and N2 adsorption into amine-functionalized metal-substituted MIL-101 frameworks using molecular simulation. *Fuel* **2022**, *308*, 121965.

(25) Teo, H. W. B.; Chakraborty, A.; Kayal, S. Evaluation of CH4 and CO2 adsorption on HKUST-1 and MIL-101(Cr) MOFs employing Monte Carlo simulation and comparison with experimental data. *Applied Thermal Engineering* **2017**, *110*, 891-900.

(26) Liu, D.; Lin, Y. S.; Li, Z.; Xi, H. Adsorption and separation of CH4/H2 in MIL-101s by molecular simulation study. *Chemical Engineering Science* **2013**, *98*, 246-254.

(27) Sun, Y.; Spellmeyer, D.; Pearlman, D. A.; Kollman, P. Simulation of the solvation free energies for methane, ethane, and propane and corresponding amino acid dipeptides: a critical test of the bond-PMF correction, a new set of hydrocarbon parameters, and the gas phase-water hydrophobicity scale. *Journal of the American Chemical Society* **1992**, *114* (17), 6798-6801.

(28) El-Sheikh, S. M.; Barakat, K.; Salem, N. M. Phase transitions of methane using molecular dynamics simulations. *The Journal of Chemical Physics* **2006**, *124* (12).

(29) Yoon, J. W.; Chang, H.; Lee, S.-J.; Hwang, Y. K.; Hong, D.-Y.; Lee, S.-K.; Lee, J. S.; Jang, S.; Yoon, T.-U.; Kwac, K.; et al. Selective nitrogen capture by porous hybrid materials containing accessible transition metal ion sites. *Nature Materials* **2017**, *16* (5), 526-531.

(30) Pillai, R. S.; Yoon, J. W.; Lee, S.-J.; Hwang, Y. K.; Bae, Y.-S.; Chang, J.-S.; Maurin, G. N2 Capture Performances of the Hybrid Porous MIL-101(Cr): From Prediction toward Experimental Testing. *The Journal of Physical Chemistry C* **2017**, *121* (40), 22130-22138.

(31) Zhang, Y.; Su, W.; Sun, Y.; Liu, J.; Liu, X.; Wang, X. Adsorption Equilibrium of N2, CH4, and CO2 on MIL-101. *J. Chem. Eng. Data* **2015**, *60* (10), 2951-2957.

(32) Li, Q.; Yuan, C.; Zhang, G.; Liu, J.; Zheng, Y. Effects of doping Mg2+ on the pore structure of MIL-101 and its adsorption selectivity for CH4/N2 gas mixtures. *Fuel* **2019**, *240*, 206-218.

(33) Kaiser, L. G.; Meersmann, T.; Logan, J. W.; Pines, A. Visualization of gas flow and diffusion in porous media. *Proceedings of the National Academy of Sciences* **2000**, *97* (6), 2414-2418.

(34) Forse, A. C.; Colwell, K. A.; Gonzalez, M. I.; Benders, S.; Torres-Gavosto, R. M.; Blümich, B.; Reimer, J. A.; Long, J. R. Influence of Pore Size on Carbon Dioxide Diffusion in Two Isoreticular Metal–Organic Frameworks. *Chemistry of Materials* **2020**, *32* (8), 3570-3576.

(35) Van de Voorde, B.; Bueken, B.; Denayer, J.; De Vos, D. Adsorptive separation on metal–organic frameworks in the liquid phase. *Chem. Soc. Rev.* **2014**, *43* (16), 5766-5788, 10.1039/C4CS00006D.

(36) Eddaoudi, M.; Sava, D. F.; Eubank, J. F.; Adil, K.; Guillerm, V. Zeolite-like metal–organic frameworks (ZMOFs): design, synthesis, and properties. *Chemical Society Reviews* **2015**, *44* (1), 228-249, 10.1039/C4CS00230J.

(37) Dubbeldam, D.; Calero, S.; Ellis, D. E.; Snurr, R. Q. RASPA: molecular simulation software for adsorption and diffusion in flexible nanoporous materials. *Molecular Simulation* **2016**, *42* (2), 81-101.

(38) Chen, Y. F.; Babarao, R.; Sandler, S. I.; Jiang, J. W. Metal−Organic Framework MIL-101 for Adsorption and Effect of Terminal Water Molecules: From Quantum Mechanics to Molecular Simulation. *Langmuir* **2010**, *26* (11), 8743-8750.

(39) Mayo, S. L.; Olafson, B. D.; Goddard, W. A. DREIDING: a generic force field for molecular simulations. *The Journal of Physical Chemistry* **1990**, *94* (26), 8897-8909.

(40) Rappe, A. K.; Casewit, C. J.; Colwell, K. S.; Goddard, W. A., III; Skiff, W. M. UFF, a full periodic table force field for molecular mechanics and molecular dynamics simulations. *Journal of the American Chemical Society* **1992**, *114* (25), 10024-10035.

(41) Dubbeldam, D.; Calero, S.; Vlugt, T. J. H. iRASPA: GPU-accelerated visualization software for materials scientists. *Mol. Simul.* **2018**, *44* (8), 653-676.

(42) Du, Z.; Nie, X.; Deng, S.; Zhao, L.; Li, S.; Zhang, Y.; Zhao, J. Comparative analysis of calculation method of adsorption isosteric heat: Case study of CO2 capture using MOFs. *Microporous and Mesoporous Materials* **2020**, *298*, 110053.

(43) Plimpton, S. Fast Parallel Algorithms for Short-Range Molecular Dynamics. *J. Comput. Phys.* **1995**, *117* (1), 1-19.

(44) LAMMPS. *pair_style lj/long/coul/long command*. 2024.

(45) LAMMPS. *pair_modify command*. 2024.

(46) García-Sánchez, A.; Dubbeldam, D.; Calero, S. Modeling Adsorption and Self-Diffusion of Methane in LTA Zeolites: The Influence of Framework Flexibility. *The Journal of Physical Chemistry C* **2010**, *114* (35), 15068-15074.

(47) Agrawal, M.; Boulfelfel, S. E.; Sava Gallis, D. F.; Greathouse, J. A.; Sholl, D. S. Determining Diffusion Coefficients of Chemical Warfare Agents in Metal–Organic Frameworks. *The Journal of Physical Chemistry Letters* **2019**, *10* (24), 7823-7830.

(48) Boyd, P. G.; Moosavi, S. M.; Witman, M.; Smit, B. Force-Field Prediction of Materials Properties in Metal-Organic Frameworks. *The Journal of Physical Chemistry Letters* **2017**, *8* (2), 357-363.

(49) Wang, Z.; Zhang, Y.; Chen, S.; Fu, Y.; Li, X.; Pei, J. Molecular simulation of adsorption and diffusion of CH4 and H2O in flexible metal-organic framework ZIF-8. *Fuel* **2021**, *286*, 119342.

(50) Zhou, Z.; Mei, L.; Ma, C.; Xu, F.; Xiao, J.; Xia, Q.; Li, Z. A novel bimetallic MIL-101(Cr, Mg) with high CO2 adsorption capacity and CO2/N2 selectivity. *Chemical Engineering Science* **2016**, *147*, 109-117.

(51) Zhang, K.; Chen, Y.; Nalaparaju, A.; Jiang, J. Functionalized metal–organic framework MIL-101 for CO2 capture: multi-scale modeling from ab initio calculation and molecular simulation to breakthrough prediction. *CrystEngComm* **2013**, *15* (47), 10358-10366, 10.1039/C3CE41737A.

(52) Chowdhury, P.; Mekala, S.; Dreisbach, F.; Gumma, S. Adsorption of CO, CO2 and CH4 on Cu-BTC and MIL-101 metal organic frameworks: Effect of open metal sites and adsorbate polarity. *Microporous and Mesoporous Materials* **2012**, *152*, 246-252.

(53) Ekramipooya, A.; Valadi, F. M.; Latifi pour, M.; Rashtchian, D.; Gholami, M. R. Effect of the Pyrrolic Nitrogen Functional Group in the Selective Adsorption of CO2: GCMC, MD, and DFT Studies. *Energy & Fuels* **2021**, *35* (19), 15918-15934.

(54) Gupta, K. M.; Zhang, K.; Jiang, J. Glucose recovery from aqueous solutions by adsorption in metal–organic framework MIL-101: a molecular simulation study. *Sci. Rep.* **2015**, *5* (1), 12821.

(55) Qin, L.-Z.; Xiong, X.-H.; Wang, S.-H.; Zhang, L.; Meng, L.-L.; Yan, L.; Fan, Y.-N.; Yan, T.-A.; Liu, D.-H.; Wei, Z.-W.; et al. MIL-101-Cr/Fe/Fe-NH2 for Efficient Separation of CH4 and C3H8 from Simulated Natural Gas. *ACS Applied Materials & Interfaces* **2022**, *14* (40), 45444-45450.

(56) Pérez-Pellitero, J.; Amrouche, H.; Siperstein, F. R.; Pirngruber, G.; Nieto-Draghi, C.; Chaplais, G.; Simon-Masseron, A.; Bazer-Bachi, D.; Peralta, D.; Bats, N. Adsorption of CO2, CH4, and N2 on Zeolitic Imidazolate Frameworks: Experiments and Simulations. *Chemistry – A European Journal* **2010**, *16* (5), 1560-1571.

(57) Wu, H.; Zhou, W.; Yildirim, T. Methane Sorption in Nanoporous Metal−Organic Frameworks and First-Order Phase Transition of Confined Methane. *The Journal of Physical Chemistry C* **2009**, *113* (7), 3029-3035.

(58) Zhang, L.; Wu, G.; Jiang, J. Adsorption and Diffusion of CO2 and CH4 in Zeolitic Imidazolate Framework-8: Effect of Structural Flexibility. *The Journal of Physical Chemistry C* **2014**, *118* (17), 8788-8794.

(59) Smart, O. S.; Neduvelil, J. G.; Wang, X.; Wallace, B. A.; Sansom, M. S. P. HOLE: A program for the analysis of the pore dimensions of ion channel structural models. *J. Mol. Graph.* **1996**, *14* (6), 354-360.

(60) Yu, S.; Fangkai, Q.; Junhong, Y. Diffusion of guest molecules in coal: Insights from simulation. *Fuel* **2022**, *323*, 124295.

(61) Zhang, Z.; Wang, H.; Li, J.; Wei, W.; Sun, Y. Experimental Measurement of the Adsorption Equilibrium and Kinetics of CO2 in Chromium-Based Metal-Organic Framework MIL-101. *Adsorption Science & Technology* **2013**, *31* (10), 903-916.

(62) Sun, Z.; Zhou, S.; Li, P. Measurement of Gas Diffusion Coefficients in Cores of Fine-Grained Lithologies Considering Stress and Adsorption Effects. *ACS Omega* **2023**, *8* (38), 34720-34728.

(63) Sedighi, M.; Talaie, M. R.; Sabzyan, H.; Aghamiri, S. F. A computational investigation on the roles of binding affinity and pore size on CO2/N2 overall adsorption process performance of MOFs through modifying MIL-101 structure. *Sustainable Materials and Technologies* **2023**, *38*, e00701.

(64) Liu, J.; Li, S.; Wang, Y. Molecular Dynamics Simulation of Diffusion Behavior of CH4, CO2, and N2 in Mid-Rank Coal Vitrinite. *Energies* **2019**, *12* (19), 3744.

(65) Déroche, I.; Maurin, G.; Borah, B. J.; Yashonath, S.; Jobic, H. Diffusion of Pure CH4 and Its Binary Mixture with CO2 in Faujasite NaY: A Combination of Neutron Scattering Experiments and Molecular Dynamics Simulations. *J Phys Chem C* **2010**, *114* (11), 5027-5034.

(66) Moganty, S. S.; Baltus, R. E. Diffusivity of Carbon Dioxide in Room-Temperature Ionic Liquids. *Industrial & Engineering Chemistry Research* **2010**, *49* (19), 9370-9376.

(67) Garcés-Polo, S. I.; Villarroel-Rocha, J.; Sapag, K.; Korili, S. A.; Gil, A. A comparative study of CO2 diffusion from adsorption kinetic measurements on microporous materials at low pressures and temperatures. *Chemical Engineering Journal* **2016**, *302*, 278-286.

(68) Zhao, Y.; Feng, Y.; Zhang, X. Molecular simulation of CO2/CH4 self- and transport diffusion coefficients in coal. *Fuel* **2016**, *165*, 19-27.

(69) Chmelik, C.; van Baten, J.; Krishna, R. Hindering effects in diffusion of CO2/CH4 mixtures in ZIF-8 crystals. *Journal of Membrane Science* **2012**, *397-398*, 87-91.

(70) Chokbunpiam, T.; Fritzsche, S.; Chmelik, C.; Caro, J.; Janke, W.; Hannongbua, S. Gate Opening, Diffusion, and Adsorption of CO2 and N2 Mixtures in ZIF-8. *The Journal of Physical Chemistry C* **2016**, *120* (41), 23458-23468.

(71) Krishna, R.; van Baten, J. M. Segregation effects in adsorption of CO2-containing mixtures and their consequences for separation selectivities in cage-type zeolites. *Separation and Purification Technology* **2008**, *61* (3), 414-423.